Cellular/Molecular

# KCNQ2/3 Gain-of-Function Variants and Cell Excitability: Differential Effects in CA1 versus L2/3 Pyramidal Neurons

**Nissi Varghese,[1] Bruno Moscoso,[3] Ana Chavez,[3] Kristen Springer,[1] Erika Ortiz,[3] Heun Soh,[1] Sabato Santaniello,[2] Atul Maheshwari,[3] and Anastasios V. Tzingounis[1]**

[1]Department of Physiology and Neurobiology, University of Connecticut, Storrs, Connecticut 06269, [2]Department of Biomedical Engineering and Connecticut Institute for the Brain and Cognitive Sciences, University of Connecticut, Storrs, Connecticut 06269, and [3]Department of Neurology, Baylor College of Medicine, Houston, Texas 77030

**Gain-of-function (GOF) pathogenic variants in the potassium channels KCNQ2 and KCNQ3 lead to hyperexcitability disorders such as epilepsy and autism spectrum disorders. However, the underlying cellular mechanisms of how these variants impair forebrain function are unclear. Here, we show that the R201C variant in KCNQ2 has opposite effects on the excitability of two types of mouse pyramidal neurons of either sex, causing hyperexcitability in layer 2/3 (L2/3) pyramidal neurons and hypoexcitability in CA1 pyramidal neurons. Similarly, the homologous R231C variant in KCNQ3 leads to hyperexcitability in L2/3 pyramidal neurons and hypoexcitability in CA1 pyramidal neurons. However, the effects of KCNQ3 gain-of-function on excitability are specific to superficial CA1 pyramidal neurons. These findings reveal a new level of complexity in the function of KCNQ2 and KCNQ3 channels in the forebrain and provide a framework for understanding the effects of gain-of-function variants and potassium channels in the brain.**

*Key words:* **gain-of-function; hippocampus; KCNQ2; KCNQ3; neurological disorders; potassium channels**

**Significance Statement**

**KCNQ2/3 gain-of-function (GOF) variants lead to severe forms of neurodevelopmental disorders, but the mechanisms by which these channels affect neuronal activity are poorly understood. In this study, using a series of transgenic mice we demonstrate that the same KCNQ2/3 GOF variants can lead to either hyperexcitability or hypoexcitability in different types of pyramidal neurons [CA1 vs layer (L)2/3]. Additionally, we show that expression of the recurrent KCNQ2 GOF variant R201C in forebrain pyramidal neurons could lead to seizures and SUDEP. Our data suggest that the effects of KCNQ2/3 GOF variants depend on specific cell types and brain regions, possibly accounting for the diverse range of phenotypes observed in individuals with KCNQ2/3 GOF variants.**

## Introduction

In recent years, several studies have discovered a large number of *de novo* pathogenic variants in potassium channels that contribute to neurologic and neurodevelopmental disorders (Heyne et al., 2018; Satterstrom et al., 2020; Wang et al., 2020). Many of these variants result in gain-of-function (GOF) rather than loss-of-function (LOF) of the channels (Niday and Tzingounis, 2018; Allen et al., 2020), with the distinction between LOF and GOF being defined in terms of effects of the variants on potassium current responses in heterologous cells, i.e., LOF variants result in smaller current responses, and GOF variants result in greater current densities (Niday and Tzingounis, 2018). It is perplexing, though, how GOF variants, which lead to increased potassium channel activity and neuronal hyperpolarization, can cause seizures and hyperexcitability.

Like many other potassium channel families, the KCNQ ($K_V7$) family of voltage-gated potassium channels has been associated with multiple hyperexcitability disorders and GOF variants (Li et al., 2013; Wainger et al., 2014; Nappi et al., 2020). The KCNQ channel family consists of five members, with KCNQ2 channels being the most commonly associated with epilepsy and developmental and epileptic encephalopathy (DEE; Dirkx et al., 2020; Malerba et al., 2020; Nappi et al., 2020; Boets et al., 2022). Although most pathogenic variants of KCNQ2 are LOF, *de novo* GOF variants have been identified in severely affected KCNQ2-DEE patients, including the R201C, R144Q, and R198Q variants (Millichap et al., 2016; Mulkey et al., 2017; Miceli et al., 2022).

Received May 26, 2023; revised Aug. 9, 2023; accepted Aug. 15, 2023.

Author contributions: N.V., S.S., A.M., and A.V.T. designed research; N.V., B.M., A.C., K.S., H.S., and S.S. performed research; N.V., B.M., A.C., E.O., S.S., A.M., and A.V.T. analyzed data; N.V. wrote the first draft of the paper; N.V., B.M., A.C., S.S., A.M., and A.V.T. edited the paper; N.V. and A.V.T. wrote the paper.

This work was funded by NIH Grants NS101596 (to A.V.T.), NS108874 (to A.V.T.), NS096029 (to A.M.), and MH126953 (to A.M.) and the National Science Foundation CAREER Award 1845348 (to S.S.). We thank all members of the Tzingounis lab for discussions.

The authors declare no competing financial interests.

Correspondence should be addressed to Anastasios V. Tzingounis at anastasios.tzingounis@uconn.edu.

https://doi.org/10.1523/JNEUROSCI.0980-23.2023

The most severe GOF variant identified is the KCNQ2 variant R201C, which neutralizes the second positively charged residue (R2) of the KCNQ2 voltage sensor domain (Mulkey et al., 2017). Electrophysiological studies in heterologous cells have shown that channels formed by KCNQ2 subunits carrying the R201C variant exhibit an increased maximal current density and a strong hyperpolarizing shift in the voltage dependence of activation (Miceli et al., 2015).

The mechanisms by which KCNQ2 GOF variants lead to hyperexcitability are not fully understood. One challenge has been the counterintuitive finding that both LOF and GOF KCNQ2 variants are associated with hyperexcitability. One leading explanation for the GOF phenotype is that these variants might only dampen the excitability of interneurons because of their high input resistance (i.e., expression of GOF variants lowers the input resistance, requiring additional input to reach the firing threshold), leading to disinhibition and hyperexcitability of the excitatory network (Miceli et al., 2015). However, this model treats pyramidal neurons as uniform populations with a fixed ion channel repertoire across development, rather than a diverse group of neurons with unique output firing patterns and a developmentally dynamic clade of ion channels. Given the diversity of pyramidal neurons in the forebrain and the high level of KCNQ2 expression in that brain region, it cannot a priori be assumed that KCNQ2 GOF variants would not affect pyramidal neuron firing properties. Therefore, this study used a conditional knock-in mouse line to determine the effects of $Kcnq2^{R201C}$ GOF in excitatory neurons and compared them with a similar mouse line that constitutively expresses a recurrent $KCNQ3^{R230C}$ GOF variant (mouse numbering $Kcnq3^{R231C}$) recently identified in patients with autism spectrum disorder with or without epilepsy (Sands et al., 2019).

## Materials and Methods

All experiments were performed according to the guidelines described in the National Institutes of Health *Guide for the Care and Use of Laboratory Animals* and were approved by the Institutional Animal Care and Use Committee of the University of Connecticut, Storrs and of Baylor College of Medicine.

### *Animals*

All mice used in this study were housed in a 12/12 h light/dark cycle with access to standard chow food and water *ad libitum*.

$Kcnq2^{R201C}$ conditional knock-in mice were generated using the Cre-lox Flip excision switch method by the Center for Mouse Genomic Modification (CMGM) at UConn Health (Farmington, CT). In this mouse line, $Kcnq2^{cR201C}$, a mutated exon 4 (mEx4) is inverted and placed in the intron between exon four and exon five flanked by a series of LoxP sites (LoxP and Lox2372). $Kcnq2^{+/cR201C}$ mice were then crossed with either the Emx1-IRES-Cre ($Emx1^{cre}$; RRID:IMSR_JAX:005628) or the ubiquitin C (UBC)-Cre-ERT2 (RRID:IMSR_JAX:007001) recombinase strain from the Jackson Laboratory for the generation of $Emx1^{cre}$::$Kcnq2^{+/cR201C}$ and $Ubc^{(Cre\text{-}ERT2/+)}$::$Kcnq2^{+/cR201C}$ mice, respectively. $Emx1^{cre/+}$::$Kcnq2^{+/+}$ mice were used as control mice and $Emx1^{cre/+}$::$Kcnq2^{+/cR201C}$ were treated as knock-in mice. For genotyping purposes, we used two sets of primers for the $Kcnq2^{+/cR201C}$ mice. The first set included F1 (5′-CCAACTCCAAGTCGGTGGGATC-3′) and R1 (5′-CAGGCAGAGTATCGATCCAGGC-3′) for identifying the 136-bp conditional knock-in. The second set included F2 (5′-GAGT TGGGTCTGGGGAGAGAG-3′) and R2 (5′-GTGTCCAGGAGAGA CTGCCCAG-3′) for identifying the wild-type (WT) and heterozygous mutants ($Kcnq2^{+/+}$, 172 bp; $Kcnq2^{+/cR201C}$, 235 bp; $Kcnq2^{+/R201C}$, 263 bp). We note, that the insertion of such a large construct between exon four and exon five led to mis-splicing. Hence, in the absence of Cre recombinase, the $Kcnq2^{+/cR201C}$ mice act as a heterozygous null. Thus, for this work we only compared animals with ($Emx1^{cre}$::$Kcnq2^{+/cR201C}$) and without ($Emx1^{cre}$::$Kcnq2^{+/+}$) the $Kcnq2^{cR201C}$ allele.

The $Kcnq3^{+/R231C}$ mice were generated using CRISPR/Cas9 endonuclease-mediated genome editing at the University of Rochester transgenic mouse facility. A guide RNA (5′-GAAGCGAAGGCTTCGCA GGG AGG-3′) was selected to target exon four of the potassium voltage-gated channel, *Kcnq3* on chromosome 8. Donor DNAs were created encoding an R231C mutation (CGC to TGC, arginine to cysteine). These sequences and Cas9 nuclease were introduced into C57BL/6J zygotes, and then transferred to pseudopregnant females. Progeny were screened by DNA sequencing of the targeted region. A founder was bred to C57BL/6J mice (RRID:IMSR_JAX:000664) for germline transmission. After establishing germline transmission, mice were transferred to the CMGM for rederivation to the C57BL6J background. Constitutive *Kcnq3* knock-out mice and genotyping have been described previously (Kim et al., 2016; Gao et al., 2021). Genotyping for $Kcnq3^{+/R231C}$ mice was performed using the following primers: *Kcnq3* wtF (5′-GGCAGTT GACATCACCCTCAACACAACTGCT-3′), *Kcnq3* wtR (5′-GACCTA AGCTCAGGTTTGCCTGTGGTCT-3′), *Kcnq3* mtF (5′- CTTGGCCA CTTCCCTGAGGAGTCTCT-3′), and *Kcnq3* mtR (5′-GCAGGATC TGCAGGAAGCAGAGACTCCt-3′**;** 5′ PCR *Kcnq3* wtF + *Kcnq3* mtR: 252 bp; 3′ PCR: *Kcnq3* mtF + *Kcnq3* wtR: 325 bp). *Kcnq3* wild-type littermates were identified using primers Forward (5′-CCACCTC CCTGCGAAG-3′) and Reverse (5′-ACCTAAGCTCAGGTTTGCC-3′) – (*Kcnq3* F + *Kcnq3* R: 319 bp)

### *Sanger sequencing and quantitative PCR*

Mouse brains from both sexes were dissected out and mRNA was isolated using the Direct-zol™ RNA MiniPrep Plus kit (catalog #R2070). A total of 0.5 µg of mRNA was used to make cDNA according to instructions from the QIAGEN RT² First Strand kit 50 (catalog #330404) kit. The cDNA was amplified using primers that targeted exon 4 (mKCNQ2 562F, 5′-CTGATTGCCTCCATTGCTG-3′; mKCNQ2 679R, 5′-CGTA GACTACGGATCCCAAG-3′) and then sent for Sanger sequencing. For quantitative PCR experiments, we used primers for *Kcnq2* (F, 5′-AG AGTCTTGATGACAGCCCGAGCAA-3′ and R, 5′-GGTAAGATCTT CAGTCACAAACTCGCA-3′), *Kcnq3*; F, 5′-CACCGTCAGAAGCAC TTTGAG-3′ and R, 5′-CCTTTAGTATTGCTACCACGAGG-3′; Robbins et al., 2013) and *Kcnq5* (F, 5′-TGGTCTGCAGGTTGCTGTTGTCGT-3′ and R, 5′-GGATCTGTAGGAACCGGAGACTTCT-3′).

### *Tamoxifen injections*

We dissolved 4-OH tamoxifen (Sigma H7904, FW:387.51) as a 10 mg/ml solution of 19:1 canola oil: ethanol. We used a water bath sonicator to dissolve the ingredients and stored the solution at 4°C. We injected 0.05 ml of tamoxifen intraperitonially to ~10-g mice using a 30-G needle. The doses were adjusted according to the weight of the mouse. Injections were given once a day for 5 d. The tamoxifen solution was sonicated before each use.

### *Acute brain slice preparation*

For all electrophysiological experiments, postnatal day (P)14–P21 mice of either sex were used. Mice anesthetized with isoflurane were rapidly killed by decapitation, and then the brains were dissected out and placed in ice-cold cutting solution (26 mM $NaHCO_3$, 1.25 mM $NaH_2PO_4$, 2.5 mM KCl, 0.5 mM $CaCl_2$, 7 mM $MgCl_2$, 10 mM dextrose, and 210 mM sucrose). To gain access to the hippocampal and cortical areas, 300-µm slices were cut coronally using a vibrating microtome (Leica VT1200S). Slices were then transferred to a holding chamber containing artificial CSF (ACSF) consisting of 125 mM NaCl, 2.5 mM KCl, 1.3 mM $MgCl_2$, 1 mM $NaH_2PO_4$, 26 mM $NaHCO_3$, and 12 mM dextrose, with 1.5 mM $CaCl_2$ added on the day of recordings. The cutting solution and ACSF were continuously saturated with 95% $O_2$ and 5% $CO_2$. Brain slices in ACSF were incubated in a 37°C water bath for 30 min, followed by room temperature for at least 1 h before the recordings. The slices were then transferred to a recording chamber, with the temperature maintained at 30–32°C using a temperature controller (Warner Instruments, TC 324C). ACSF was continuously perfused into the chamber by a peristaltic pump.

### *Electrophysiological recordings*

We used 2- to 4-MΩ borosilicate glass electrodes to perform whole-cell recordings. Current clamp recordings were performed on layer (L)2/3

pyramidal neurons of the somatosensory cortex and CA1a pyramidal neurons of the hippocampus. CA1a superficial and deep neurons were identified based on their position within the CA1 pyramidal cell layer. Specifically, superficial neurons are located closer to stratum radiatum, while deep neurons are positioned closer to stratum oriens (Masurkar et al., 2020). L2/3 pyramidal neurons were identified at the dense region of neurons below the pia (~200 μm), and their regular spiking firing activity. Recording pipettes were filled with an internal solution consisting of 130 mM $CH_3KO_4S$, 10 mM KCl, 4 mM NaCl, 4 mM Tris-phosphocreatine, 10 mM HEPES, 4 mM Mg-ATP, and 0.4 mM Na-ATP. L2/3 neuronal recordings were conducted in the presence of synaptic blockers consisting of 100 $\mu$M picrotoxin to block $GABA_A$ receptor-mediated inhibitory responses, 4 $\mu$M NBQX to block AMPA-mediated responses, and 10 $\mu$M D-AP5 to block NMDA-mediated responses. This was necessary to obtain stable baseline activity. All current clamp recordings for CA1 and L2/3 pyramidal neurons were made using a Multiclamp 700B amplifier (Molecular Devices) with bridge balancing and pipette capacitance neutralization engaged. Cells with access resistance <20 MΩ were considered for recording and analysis. To assess intrinsic excitability and action potential waveform properties, we used a depolarizing current injection from +25 to +325 pA with +Δ25-pA current steps (13 sweeps) with a step lasting for 1- and 15-s intervals in between the sweeps. To determine the cell's input resistance, we used a series of hyperpolarizing steps ranging from −100 to 0 pA with, Δ25-pA current step interval (five sweeps). Each hyperpolarizing step lasted 1 s with no intervals between the sweeps. Resting membrane potential was measured at I = 0 soon after break into the cell. To compare the firing properties between CA1 and L2/3 pyramidal neurons we set the holding membrane potential at ~−65 mV before initiation of the step or ramp protocols. We sampled data at a rate of 50 kHz (every 20 μs) and the Bessel filter was set to 10 kHz. All voltage clamp experiments were sampled at a rate of 10 kHz and a Bessel filter of 2 kHz. For M-current measurements 500 nM TTX, 1 mM cesium, 2 mM 4-AP, and 100 $\mu$M cadmium we also added to the extracellular solution. Data acquisition of all electrophysiology experiments was conducted using Digidata 1440 A and pClamp software (10.2–11.2; RRID:SCR_011323).

In vivo *video-EEG monitoring*

Electrode implantation was performed using standard procedures as described previously (Jing et al., 2022). Mice of either sex and at least 30 d old were anesthetized with isoflurane and prepared in a sterile field. Teflon-coated twisted silver wire electrodes (25 $\mu$m in diameter, Omnetics Inc.) were placed stereotactically in the epidural space over the bilateral medial frontal cortex (1 mm anterior and lateral to the bregma) and bilateral parietal cortex (2.5 mm posterior and 1.5 mm lateral to the bregma). For two wild-type and three mutant mice, the parietal electrodes were replaced by stereotactically placed hippocampal depth electrodes targeting CA3 (2.0 mm posterior, 1.8 mm lateral and 1.8 mm deep to bregma; You et al., 2017). Reference and ground electrodes were placed over the left and right cerebellum, respectively. One hour after recovery, freely moving mice were recorded using continuous video-EEG monitoring (AD Instruments) for at least 2 h daily as long as they survived. The EEG power spectra were calculated using the spectral analysis function [spectropo()] in EEGLab (Delorme and Makeig, 2004). Seizures were detected by visual inspection.

*NEURON models*

We considered a multicompartmental conductance-based model of pyramidal neuron from the Blue Brain Project (BBP) portal (Markram et al., 2015; Ramaswamy et al., 2015). The model morphology includes soma, apical and basal dendrites, and axon obtained from 3D digital reconstruction of a biocytin-filled neuron from a slice of somatosensory cortex. Up to 13 different types of ion channels, including $Ca^{2+}$-activated $K^+$ channels ($SK_v3.1$), high-voltage-activated $Ca^{2+}$ channels, persistent $K^+$ and $Na^+$ channels, HCN-current, and M-current (Kv7/KCNQ channels), were included in the model compartments, with the channel maximum conductance fit on experimental data via a multiobject optimization routine (Druckmann et al., 2007).

To match the electrophysiology of the WT P14 mouse (i.e., control case), we modified the original model from the BBP portal by adding M-currents to the soma and axon initial segment (AIS, max conductance, $g_{max} = 7.4 \times 10^{-4}$ S/cm$^2$ and $g_{max} = 7.4 \times 10^{-3}$ S/cm$^2$, soma and AIS, respectively) and lowering the maximum conductance of $SK_v3.1$ channels in the soma (i.e., $2.05 \times 10^{-2}$ S/cm$^2$ instead of $1.02 \times 10^{-1}$ S/cm$^2$) and persistent $K^+$ currents in the axonal compartments (i.e., $5.76 \times 10^{-1}$ instead of $9.59 \times 10^{-1}$ S/cm$^2$). The M-current model was as in (Markram et al., 2015), i.e.,

$$I_M = g_{max} m (V - E_K)$$

$$\frac{dm}{dt} = \frac{m_\infty(V) - m}{\tau_m},$$

where $I_M$ is the M-current, $E_K$ is the $K^+$ Nernst equilibrium potential, $m_\infty = \alpha/(\alpha+\beta)$, and $\tau_m = 1/(\alpha+\beta)$, with functions $\alpha = 3.3 \times 10^{-3} \exp(0.04w(V - V_t))$ and $\beta = 3.3 \times 10^{-3} \exp(-0.04w(V - V_t))$. Parameters $V_t$ and w control the half-activation value and the slope of the conductance-voltage curve of the M-current, respectively, and were kept at −35 mV and 2.5, respectively, in the control case. Identical channel assembly throughout the neuron model was assumed, and the parameters of the M-current were accordingly kept uniform across the various model compartments.

To simulate the effects of KCNQ2/3 GOF on the M-current, we set $V_t = -45$ mV and $w = 3.5$, which resulted in decreasing the half-activation current by 10 mV and increasing the slope of the conductance-voltage curve as reported in (Miceli et al., 2015). In addition, we increased the maximum conductance of the M-current (i.e., $g_{max}$ was set to twice the value in the *control* case) selectively in the soma (*soma*), soma and apical dendrites (*soma+apical*), soma and AIS (*soma+AIS*), or all compartments (*soma+apical+AIS*). For each configuration, the model was adjusted for a temperature $T = 30$°C and simulated in NEURON, version 8.2 (Carnevale and Hines, 2006) for 2500 ms (solver: CVODE; integration step: 0.02 ms). In each simulation, the resting membrane potential was initialized at −65 mV, and a step current was applied to the soma (onset: 500 ms; duration: 1000 ms) with intensity up to +325 pA to match the experiments. The firing rate was then calculated as the resultant number of evoked action potentials. The action potential rate of rise and decay (in mV/ms) was calculated as the first derivative (i.e., slope) of the somatic transmembrane voltage. We defined the rate of rise of an action potential as the most positive slope value preceding the peak of the action potential, and we defined the rate of decay of an action potential as the most negative slope value immediately following the peak of the action potential. We looked at the rate of rise and decay as the amplitude of the injected step-current is varied from +25 pA to +325 pA for three different scenarios: control, which corresponds to the wild-type condition, and the scenarios where the GOF mutants are expressed at the soma, axon initial segment, and apical dendrite (i.e., *soma+AIS+apical*), either uniformly or nonuniformly.

*Experimental design and statistical analyses*

All data are shown as mean ± SEM. The sample sizes used in the study were based on our previous experience with similar studies (Soh et al., 2014, 2018; Niday et al., 2017). All data were analyzed offline using Clampfit 11.2 and summary graphs and representative images were generated using GraphPad Prism 9.5 (RRID:SCR_002798) or IGOR Pro (RRID:SCR_000325). Two-sided unpaired Student's *t* tests were used for comparison of two groups as well as two-way repeated measures or mixed effects ANOVAs for multiple group comparisons for statistical significance. Area under the curve analysis were executed for all frequency curves. Initial *in vivo* recordings were done with knowledge of genotype, but review of seizures was done after blinding. All statistical analyses were performed in GraphPad Prism 9.5 (RRID:SCR_002798). *p* values of <0.05 were considered statistically significant. In figure legends and Results, *n* indicates number of cells, whereas *N* indicates number of animals.

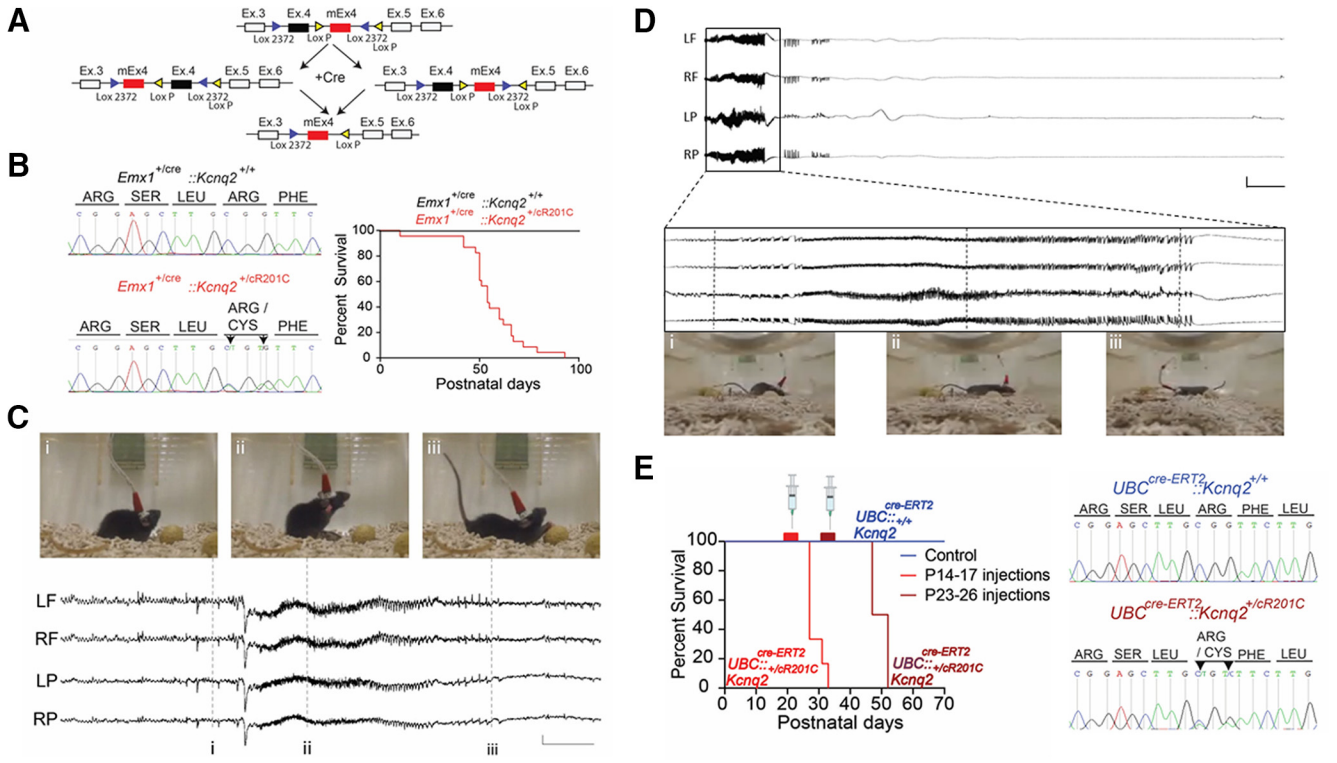


**Figure 1.** Expression of KCNQ2 R201C GOF variant in forebrain excitatory neurons lead to premature lethality, tonic-clonic seizures, and SUDEP. ***A***, Illustration of the design of the $Kcnq2^{+/cR201C}$ mice and the effect of expression of Cre recombinase. ***B***, Sequencing validation of expression of $Kcnq2^{R201C}$ transcript in $Emx1^{cre}$::$Kcnq2^{+/cR201C}$ mice and survival curves of $Emx1^{cre/+}$::$Kcnq2^{+/+}$ (black, $n = 10$) and $Emx1^{cre/+}$::$Kcnq2^{+/cR201C}$ (red, $n = 16$; Kaplan Meier $p < 0.0001$). We observed that mice expressing one copy of $Kcnq2^{R201C}$ die prematurely. ***C***, Video-electrocorticography (ECoG) recordings of $Kcnq2^{R201C}$ GOF mice show presence of spontaneous tonic-clonic seizures, starting with behavioral arrest (i), followed by a tonic phase (ii), and culminating in a clonic phase with tonic hindlimb extension (iii). Simultaneous ECoG shows intermittent generalized spikes (i) followed by low-voltage fast activity with a direct current [DC] shift (ii) followed by rhythmic generalized spikes before seizure termination (iii). LF = left frontal, RF = right frontal, LP = left parietal, RP = right parietal. Scale bar = 100 $\mu$V and 5 s. ***D***, Sudden unexpected death in epilepsy (SUDEP) event captured with video-EEG monitoring with brain death following a tonic clonic seizure, including (i) behavioral arrest with low-voltage fast activity, (ii) a tonic phase, and then (iii) a clonic phase with generalized spikes before seizure termination and death (horizontal scale = 12 s, 1 s in inset; vertical scale = 200 $\mu$V, 100 $\mu$V in inset). ***E***, Global expression of $KCNQ2^{R201C}$ GOF variant leads to premature lethality. Left, survival curves of $UBC^{cre\text{-}ERT2}$::$Kcnq2^{+/cR201C}$ and $UBC^{cre\text{-}ERT2}$::$Kcnq2^{+/+}$. We found that mice expressing one copy of $Kcnq2^{R201C}$ die prematurely two weeks after tamoxifen injection. Right, sanger sequencing validation of expression of $Kcnq2^{R201C}$ in $UBC^{cre\text{-}ERT2}$::$Kcnq2^{+/cR201C}$ mice 12 d after tamoxifen injection.

## Results

### $Kcnq2^{+/R201C}$ expression leads to premature lethality

Our main goal was to investigate whether KCNQ2 GOF affects the excitability of forebrain pyramidal neurons. For this, we used a mouse line ($Kcnq2^{+/cR201C}$) conditionally expressing $Kcnq2^{R201C}$ in neurons when Cre recombinase is present. In cells with Cre recombinase, the inverted mEx4 is flipped and the wild-type exon four is excised, resulting in the expression of one copy of wild-type exon four and one copy of mEx4 ($Kcnq2^{+/R201C}$; Fig. 1*A*). Using the $Emx1^{cre}$ line, we sequenced exon four to determine the expression of mEx4 across the forebrain in $Emx1^{cre}$::$Kcnq2^{+/cR201C}$ mice. As Emx1 allows for the expression of Cre recombinase starting at embryonic day 10.5 (E10.5) in excitatory forebrain neurons (Gorski et al., 2002), we expected to detect $Kcnq2^{R201C}$ across the forebrain by postnatal day 15 (P15). Indeed, our sequencing results confirmed the presence of mEx4 in our $Emx1^{cre}$::$Kcnq2^{+/cR201C}$ heterozygous mice (Fig. 1*B*).

To determine whether the levels of *Kcnq2* differ between the $Emx1^{cre}$::$Kcnq2^{+/+}$ and $Emx1^{cre}$::$Kcnq2^{+/cR201C}$ lines, we conducted quantitative PCR. For the remainder of the manuscript, we refer to $Emx1^{cre}$::$Kcnq2^{+/cR201C}$ as $Kcnq2^{+/R201C}$ and $Emx1^{cre}$::$Kcnq2^{+/+}$ as $Kcnq2^{+/+}$. We found that the transcript levels of *Kcnq2*, as well as *Kcnq3* and *Kcnq5*, remained similar between the two lines (Normalized to $Kcnq2^{+/+}$, *Kcnq2*: $Kcnq2^{+/R201C} = 1.05 \pm 0.13$, $N = 3$; *Kcnq3*: $Kcnq2^{+/R201C} = 1.1 \pm 1.9$, $N = 3$; *Kcnq5*: $Kcnq2^{+/R201C} = 0.89 \pm 0.12$, $N = 3$). Despite this, $Kcnq2^{+/R201C}$ mice expressing one copy of $Kcnq2^{R201C}$ in the forebrain showed premature lethality, beginning as early as P40, with almost complete lethality by P100 (Fig. 1*B*). Similarly, in a separate colony almost all $Kcnq2^{+/R201C}$ mice (mice with one copy of Cre and one copy of $Kcnq2^{+/R201C}$) were found dead between P30 and P80 (Baylor College of Medicine), similar to the original (University of Connecticut) cohort (Fig. 1*B*). We also discovered that these mice exhibited tonic-clonic seizures (Fig. 1*C*) and SUDEP (Fig. 1*D*). Taken together, our findings suggest that the expression of a KCNQ2 GOF variant in excitatory neurons may result in network hyperexcitability.

To further examine the effect of $Kcnq2^{R201C}$ in mice, we used ubiquitin C (UBC)-Cre-ERT2 mice to drive expression of Cre recombinase to achieve global expression of the variant. This approach was necessary because the constitutive expression of one copy of $Kcnq2^{R201C}$ resulted in perinatal death, occurring shortly after birth. In UBC-Cre-ERT2 mice, Cre recombinase is under control of the UBC promoter, and its induction is triggered following administration of tamoxifen (Fig. 1*E*). We found that administration of tamoxifen caused the mice to die within two weeks, regardless of whether Cre recombinase induction was activated two or three weeks postbirth (Fig. 1*E*). Therefore, expression of KCNQ2 GOF variants results in a highly severe phenotype, comparable to the effects in *Kcnq2* knock-out mice shown in previous work (Soh et al., 2014).

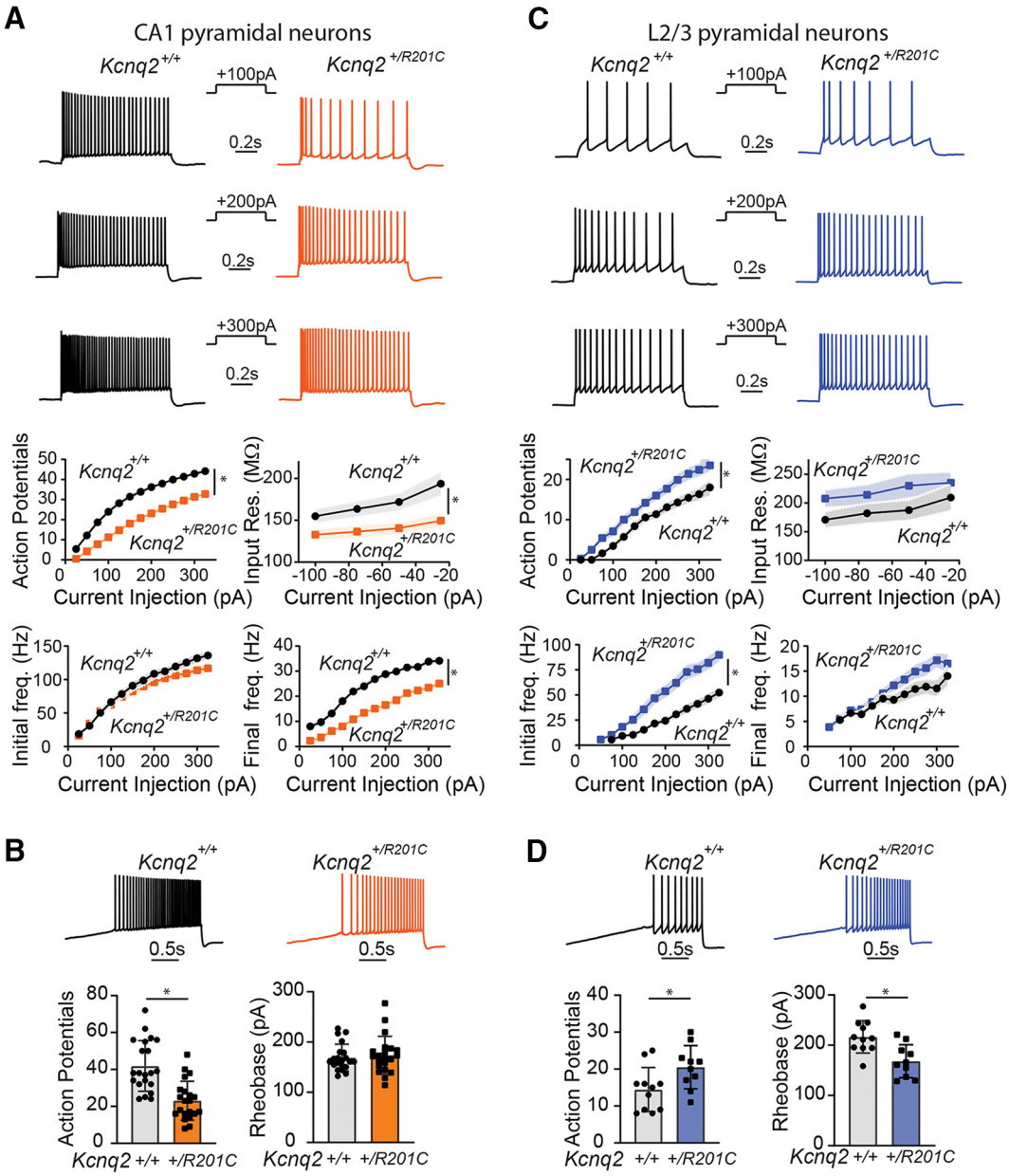


**Figure 2.** KCNQ2$^{R201C}$ leads to hypoexcitability of CA1 pyramidal neurons and hyperexcitability of L2/3 pyramidal neurons. ***A***, Top, Representative voltage responses in response to different depolarizing current injections (1 s) in CA1 pyramidal neurons. Bottom, Summary graphs showing the effects of one copy of *Kcnq2*$^{R201C}$ variant to CA1 pyramidal neurons action potential count, initial frequency and final frequency, and input resistance (*Kcnq2*$^{+/+}$: $n = 21$, $N = 9$; *Kcnq2*$^{+/R201C}$: $n = 23$, $N = 8$). ***B***, Representative voltage responses to +120-pA/s ramp protocol from *Kcnq2*$^{+/+}$ (black) and *Kcnq2*$^{+/R201C}$ (orange) CA1 pyramidal neurons. Summary graphs showing the effects on action potential number and rheobase (*Kcnq2*$^{+/+}$: $n = 21$, $N = 9$; *Kcnq2*$^{+/R201C}$: $n = 21$, $N = 8$). ***C***, Top, Representative voltage responses in response to different depolarizing current injections (1 s) in L2/3 pyramidal neuron. Bottom, Summary graphs showing the effects of one copy of *Kcnq2*$^{R201C}$ variant to L2/3 pyramidal neurons action potential count, initial and final frequency, as well as input resistance (*Kcnq2*$^{+/+}$: $n = 11$, $N = 3$; *Kcnq2*$^{+/R201C}$: $n = 10$, $N = 3$). ***D***, Representative voltage responses to +120-pA/s ramp protocol from *Kcnq2*$^{+/+}$ (black) and *Kcnq2*$^{+/R201C}$ (blue) L2/3 pyramidal neurons. Summary graphs showing the effects on action potential number, and rheobase (*Kcnq2*$^{+/+}$: $n = 11$, $N = 3$; *Kcnq2*$^{+/R201C}$: $n = 10$, $N = 3$). Summary graphs show mean and SEM. * indicates $p < 0.05$. Detailed statistics are found in Table 2.

### The KCNQ2 R201C variant leads to hypoexcitability of CA1 pyramidal neurons and hyperexcitability of layer 2/3 (L2/3) pyramidal neurons

Based on the findings mentioned above, we hypothesized that the KCNQ2$^{R201C}$ variant might alter the firing characteristics of hippocampal CA1 and neocortical L2/3 pyramidal neurons. These neuronal types are responsive to changes in KCNQ2 levels, and previous work using *Kcnq2* knock-out mice has shown that ablation of *Kcnq2* from forebrain excitatory neurons increases the excitability of CA1 (Soh et al., 2014) and L2/3 pyramidal neurons (Niday et al., 2017). We conducted whole-cell patch current clamp recordings in both CA1 and L2/3 pyramidal neurons. We held both cells at a potential of ~−65 mV and injected depolarizing current steps of increasing magnitude, measuring the resulting number of action potentials and the firing frequency (Fig. 2).

Figure 2*A* shows the action potential count, initial firing frequency (i.e., frequency of the first two action potentials), and final firing frequency (i.e., frequency of the last two action potentials) as a function of the injected current. Our findings revealed that CA1 pyramidal neurons expressing KCNQ2$^{R201C}$ are hypoexcitable. Specifically, the number of action potentials and the

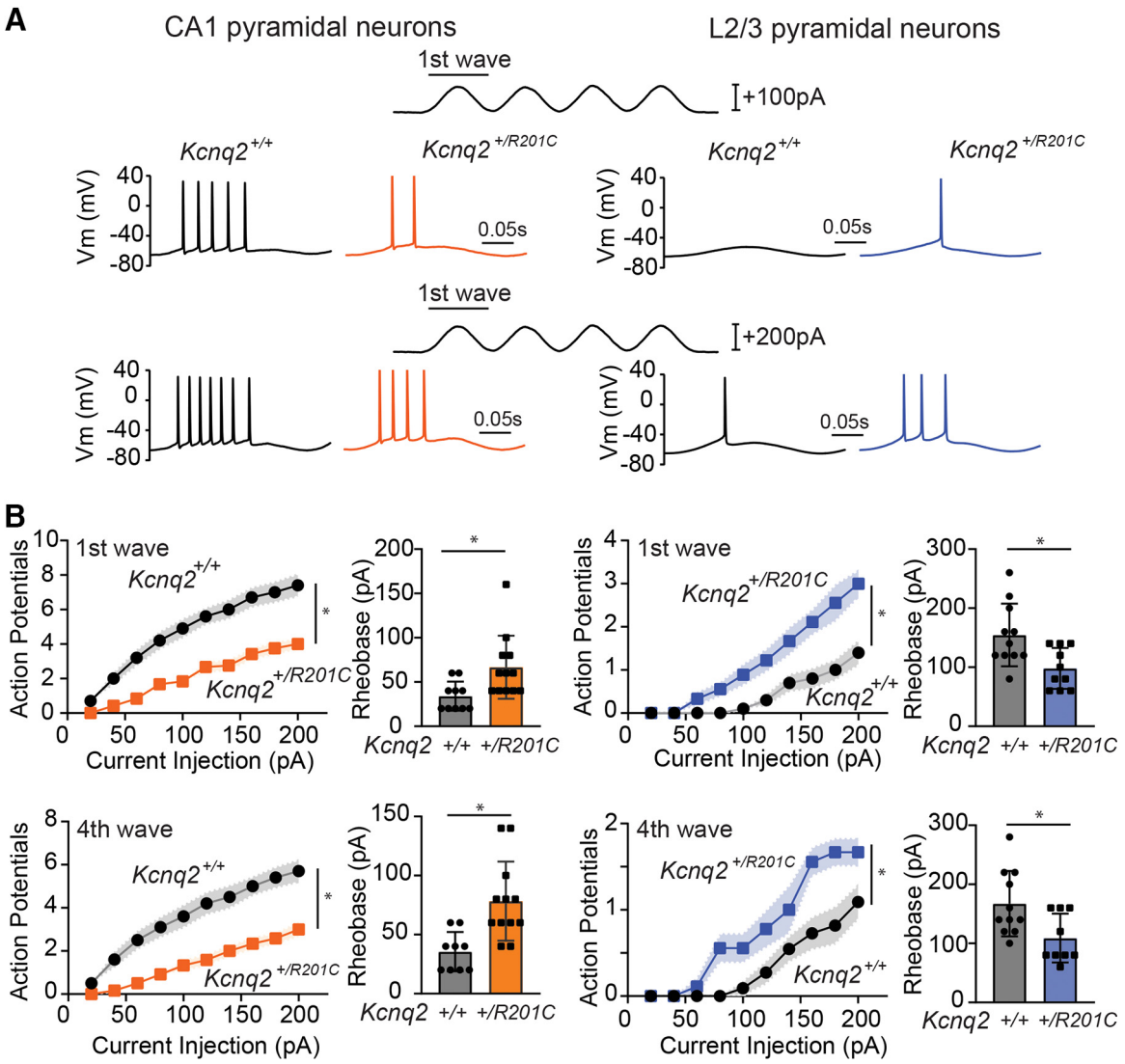


**Figure 3.** KCNQ2$^{R201C}$ leads to hypoexcitability of CA1 pyramidal neurons and hyperexcitability of L2/3 pyramidal neurons independent of the protocol. ***A***, Representative voltage responses to the first wave of the four sinusoidal cycles (+100 pA, top, and +200 pA, bottom) for *Kcnq2*$^{+/+}$ (black) and *Kcnq2*$^{+/R201C}$ mice in CA1 and L2/3 pyramidal neurons (orange and blue). ***B***, Summary graphs of action potential count for the first and fourth wave of CA1 pyramidal neurons (*Kcnq2*$^{+/+}$: $n = 10$, $N = 3$; *Kcnq2*$^{+/R201C}$: $n = 12$, $N = 4$) and L2/3 pyramidal neurons (*Kcnq2*$^{+/+}$: $n = 11$, $N = 3$; *Kcnq2*$^{+/R201C}$: $n = 10$, $N = 3$) as well as the corresponding rheobase currents. Summary graphs show mean and SEM. * indicates $p < 0.05$. Detailed statistics are found in Table 2.

steady-state firing frequency were significantly decreased in CA1 pyramidal neurons of *Kcnq2*$^{+/R201C}$ mice. Upon closer examination of our data, we discovered that CA1 pyramidal neurons from *Kcnq2*$^{+/R201C}$ mice had lower input resistance (Fig. 2*A*). This reduced input resistance of CA1 pyramidal neurons was consistent with a greater number of KCNQ2 channels being open at rest either at the soma or AIS. To confirm our findings, we also assessed the firing behavior of CA1 pyramidal neurons using a slow ramp protocol (120 pA/s). As shown in Figure 2*B*, KCNQ2$^{R201C}$-expressing neurons showed fewer action potentials. Hence, our results are consistent with those of the step protocol, indicating that CA1 pyramidal neurons of *Kcnq2*$^{+/R201C}$ mice are hypoexcitable regardless of the stimulation protocol. In contrast to our observations in CA1 pyramidal neurons, we found that KCNQ2$^{R201C}$-expressing L2/3 pyramidal neurons displayed hyperexcitability. Specifically, we observed an increase in both the number of action potentials, the initial, and steady-state firing frequency in response to injected currents (Fig. 2*C*), and a slightly higher input resistance (Fig. 2*C*). The increased number of action potentials was also evident in our slow ramp protocol data (Fig. 2*D*), which further confirmed the hyperexcitability of the L2/3 pyramidal neurons.

To further compare the excitability of CA1 and L2/3 pyramidal neurons, we used a sinusoidal protocol that mimicked 4-Hz EPSP-like waveforms. As expected, CA1 pyramidal neurons were hypoexcitable while L2/3 pyramidal neurons were hyperexcitable, whether measured during the first EPSP-like wave or the fourth EPSP-like wave (Fig. 3*A*,*B*). This difference was also reflected in the rheobase, with an observed decrease in L2/3 pyramidal neurons and increase in CA1 pyramidal neurons (Fig. 3*B*). We note that expression of KCNQ2$^{R201C}$ did not change the somatic resting membrane potential of either CA1 or L2/3 pyramidal neurons (CA1 Vrest: *Kcnq2*$^{+/+}$ $-60 \pm 1.5$ mV, $n = 10$, $N = 3$; *Kcnq2*$^{+/R201C}$ $-62 \pm 2.6$ mV, $n = 7$, $N = 2$; L2/3 Vrest: *Kcnq2*$^{+/+}$ $-77.6 \pm 1.7$ mV, $n = 11$, $N = 3$; *Kcnq2*$^{+/R201C}$ $-74.7 \pm 3.4$ mV, $n = 10$, $N = 3$).

The results from our L2/3 pyramidal neuron experiments raised the possibility that the increased firing activity of L2/3 pyramidal neurons might be because of a loss of KCNQ-mediated currents, such as the M-current, rather than a GOF effect. To

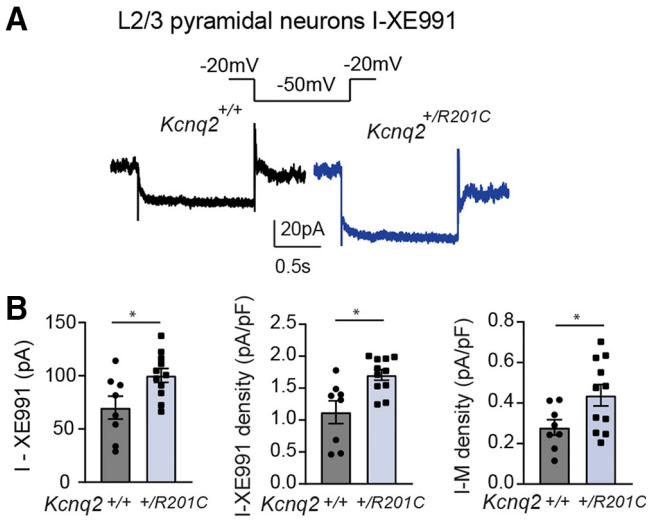


**Figure 4.** KCNQ2$^{R201C}$-expressing L2/3 pyramidal neurons have greater M-current. ***A***, Panel shows the M-current protocol and representative XE991-sensitive KCNQ-current traces in L2/3 pyramidal neurons (*Kcnq2*$^{+/+}$: $n = 8$, $N = 3$; *Kcnq2*$^{+/R201C}$: $n = 11$, $N = 5$). ***B***, Summary graphs for XE991 sensitive currents, XE991 current and M-current density (deactivating current) were obtained using the traditional protocol in L2/3 pyramidal neurons of *Kcnq2*$^{+/+}$ (black) and *Kcnq2*$^{+/R201C}$ (blue) mice. Summary graphs show mean and SEM. * indicates $p < 0.05$. Detailed statistics are found in Table 2.

exclude this possibility, we recorded the M-current from L2/3 pyramidal neurons using a standard M-current protocol (Fig. 4*A*). Specifically, in the presence of a cocktail of blockers to inhibit voltage-gated sodium, calcium, and a subset of potassium channels, we held the membrane potential at −20 mV to open the KCNQ channels and inactivate A-type currents. Then, we stepped down to −50 mV to close the channels, giving rise to a slow deactivating potassium current. We measured the slow deactivating component known as the M-current and found that it was larger in *Kcnq2*$^{+/R201C}$ L2/3 pyramidal neurons (Fig. 4*B*). However, because the M-current only represents a portion of the total KCNQ-mediated currents in neurons, we repeated our experiments in the presence of the pan-KCNQ blocker XE991. We found that the XE991-sensitive current density was larger in L2/3 pyramidal neurons from *Kcnq2*$^{+/R201C}$ brain slices compared with control mice (Fig. 4*B*). We note, that we assumed that at −20 mV the majority of KCNQ2/3 channels are in the open state. Consequently, any alterations in the maximum current resulting from a KCNQ2$^{R201C}$ variant should be detectable in our recordings. However, our M-current protocol might underestimate changes to the M-current near the resting membrane potential if KCNQ2$^{R201C}$ substantially shifts the KCNQ2/3 $V_{0.5}$ to hyperpolarized membrane potentials.

Therefore, our data suggest that the increased hyperexcitability of L2/3 pyramidal neurons occurs in the presence of elevated KCNQ-mediated currents. Consistent with this finding, we detected a high occurrence of spike wave discharges in *Kcnq2*$^{+/R201C}$ mice recorded before P40 *in vivo* (Fig. 5; Table 1). With *in vivo* video-EEG monitoring, generalized spike-wave discharges were captured in all six mutant mice, with four mice also demonstrating convulsive seizures. None of the five littermate *Kcnq2*$^{+/+}$ mice had any epileptiform activity captured (Table 1). Generalized spike wave discharges are a common electrographic seizure pattern that reflect neocortical pyramidal cell excitability rather than hippocampal excitability (Timofeev et al., 1998; Maheshwari and Noebels, 2014). Indeed, we did not find elevated excitability from the hippocampus in mice showing elevated spike wave discharges. This finding further demonstrates that the effect of increasing KCNQ2 currents on the excitability of pyramidal neurons depends on the cell type, leading to hypoexcitability or hyperexcitability in different cell types and regions.

### The KCNQ3 R231C variant leads to hypoexcitability of superficial CA1 pyramidal neurons and hyperexcitability of L2/3 pyramidal neurons

To determine whether our findings regarding hypoexcitability and hyperexcitability in CA1 and L2/3 pyramidal neurons are specific to KCNQ2 channels, we used the CRISPR-Cas9 system to introduce the KCNQ3$^{R230C}$ variant (equivalent to *Kcnq3*$^{R231C}$ in mice) in C57BL/6J mice. Unlike *Kcnq2*$^{+/R201C}$ mice, these mice survived to adulthood. Initial recordings of CA1 pyramidal neuron firing activity showed no significant difference between *Kcnq3*$^{+/+}$ and *Kcnq3*$^{+/R231C}$ mice (*Kcnq3*$^{+/+}$: 26 ± 3 APs, $n = 23$, $N = 11$; *Kcnq3*$^{+/R231C}$: 21 ± 3 APs, $n = 34$, $N = 16$) as well as similar resting membrane potential (CA1 Vrest: *Kcnq3*$^{+/+}$ −60 ± 0.9 mV, $n = 11$, $N = 5$; *Kcnq3*$^{+/R231C}$ −62 ± 1.7 mV, $n = 18$, $N = 8$). However, recent RNA-sequencing work has shown that the *Kcnq3* transcript levels are not uniformly expressed between the dorsal superficial and deep layers of CA1 pyramidal neurons (Deep: 61.9 ± 5.1 fkpm; Superficial: 88.3 ± 5.2 fkpm, $*p = 0.022$, $t = 3.630$;df = 4), unlike *Kcnq2* transcripts (Deep: 81.9 ± 0.91 fkpm, Superficial: 82.8 ± 2.36 fkpm, $n = 3$; values obtained from https://hipposeq.janelia.org/; Cembrowski et al., 2016).

Therefore, we reanalyzed the data according to the layer of the recorded cell, which we documented during the experiments. As expected, we found that deep and superficial neurons had distinct firing properties, with deep neurons firing at higher frequency than superficial neurons (Fig. 6). Importantly, only the superficial neurons, which had higher expression of *Kcnq3* mRNA, were hypoexcitable in the presence of *Kcnq3*$^{R231C}$, firing fewer action potentials than those in control littermates (Fig. 7*A*). In contrast, the deep neurons were not affected by the expression of *Kcnq3*$^{R231C}$ (Fig. 7*B*). We further confirmed the sensitivity of superficial pyramidal neurons to KCNQ3 levels by recording from *Kcnq3* knock-out mice (Fig. 7). Our finding with *Kcnq3*$^{R231C}$ mice is different from the results we obtained with *Kcnq2*$^{+/R201C}$ mice, where neurons in both the deep and superficial layers were hypoexcitable (Fig. 8), consistent with the similar transcript levels of *Kcnq2* in both layers. Together, our findings suggest that the effect of KCNQ2/3 GOF variants on CA1 pyramidal neuron excitability may be dependent on the specific ion channel involved and its expression in different layers of the hippocampus.

Subsequently, we recorded from L2/3 pyramidal neurons of *Kcnq3*$^{+/R231C}$ mice and observed a similar effect as in *Kcnq2*$^{+/R201C}$ mice (Fig. 9). Specifically, the expression of *Kcnq3*$^{R231C}$ resulted in heightened neuronal excitability, which was reflected as an increase in the number of action potentials (Fig. 9*A*). In contrast to *Kcnq2*$^{+/R201C}$ L2/3 pyramidal neurons, we did not find any effects using the ramp protocol, suggesting that impact of *Kcnq3*$^{R231C}$ depends on the stimulus protocol (Fig. 9*B*). No difference in the somatic resting membrane potentials between the two genotypes was found (L2/3 Vrest: *Kcnq3*$^{+/+}$ −72 ± 2 mV, $n = 11$, $N = 3$; *Kcnq3*$^{+/R231C}$ −70.6 ± 2.1 mV, $n = 12$, $N = 3$), similar to the data with the *Kcnq2*$^{+/R201C}$ mice.

### Computer simulations of L2/3 neuron models suggest that increasing KCNQ current density leads to greater maximal firing activity

A question that remained unanswered is how KCNQ2/3 GOF leads to increased excitability in L2/3 pyramidal neurons. To start

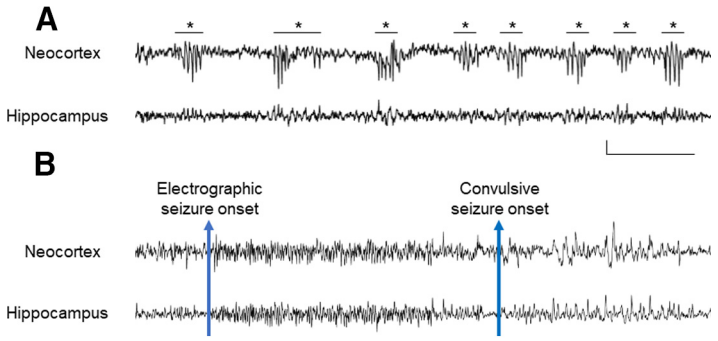


**Figure 5.** Seizure activity captured with simultaneous neocortical (epidural) and hippocampal (depth) electrode recordings. Mice were implanted with bilateral frontal (epidural) and hippocampal (depth) electrodes. ***A***, Recording from a P33 *Kcnq2*$^{+/R201C}$ mouse with frequent 1- to 2-s absence seizures (*) more prominently expressed in neocortical leads compared with hippocampal leads, associated with behavioral arrest. These are consistent with seizures in typical absence seizures, which engage neocortical more so than hippocampal circuitry. ***B***, A recording from a P40 *Kcnq2*$^{+/R201C}$ mouse with convulsive seizure activity (filtered with a 2-Hz high pass filter to better illustrate electrographic onset) associated with repetitive tonic posturing, followed by clonic convulsive activity ~12 s after electrographic seizure onset. Note the near-simultaneous onset of seizures in both neocortical and hippocampal leads; horizontal bar = 5 s, vertical bar = 250 $\mu$V.

**Table 1. Summary of seizure activity data**

| Genotype | Implant age | Electrode location | Death? | Seizures |
|---|---|---|---|---|
| *Kcnq2*$^{+/R201C}$ | P36 | Frontal; parietal | Found dead P38 | Absence seizures (day 1)<br>5 convulsive seizures (day 2) |
| | P33 | Frontal; parietal | Found dead P36 | Absence seizures (day 1)<br>7 convulsive seizures (day 2)<br>5 convulsive seizures (day 3) |
| | P47 | Frontal; hippocampal | Found dead P48 | Absence seizures (day 1) |
| | P39 | Frontal; hippocampal | Found dead P43 | Absence seizures (day 1)<br>2 convulsive seizures (day 2)<br>1 convulsive seizure (day 3) |
| | P31 | Frontal; hippocampal | SUDEP recorded P41 | No seizures (days 1–8)<br>Absence seizures (day 9)<br>Death after convulsive seizure (day 10) |
| | P33 | Frontal; hippocampal | Found dead P34 | Absence seizures (day 1) |
| *Kcnq2*$^{+/+}$ | P31 | Frontal; parietal | Survived >P80 | No seizures (days 1–3) |
| | P30 | Frontal; parietal | | |
| | P31 | Frontal; hippocampal | | No seizures (days 1–3) |
| | P38 | Frontal; hippocampal | | No seizures (days 1–3) |
| | P33 | Frontal; hippocampal | | No seizures (days 1–3) |

The table shows the number of animals that exhibit different types of seizures.

addressing this question, we used a computational approach. We employed a multicompartment model of an L2/3 pyramidal neuron from the Blue Brain Project (Markram et al., 2015; Ramaswamy et al., 2015) and we simulated a step protocol under control conditions and with increased M-current conductance in the soma, dendrites, and axon initial segment (AIS). We constrained the model such that the M-current was enriched 10-fold in the AIS relative to the dendrites and soma, as has been previously shown in L5 pyramidal neurons (Battefeld et al., 2014). To simulate the effects of M-current GOF, we increased the maximum conductance by 2-fold and shifted the $V_{0.5}$ by −10 mV (Miceli et al., 2015), a value based on the effects of KCNQ2 GOF in the presence of one copy of wild-type KCNQ2 and two copies of KCNQ3 channels (Miceli et al., 2015). We showed that changing the M-current in both the AIS and the soma could reproduce the maximal increase in firing rate observed experimentally (Fig. 10).

First, we increased the maximum conductance, $g_{max}$, for the M-current uniformly in the soma and AIS compartments (i.e., twice the value used in the control WT case) and we showed that this led to increased firing rate (Fig. 10*A*, top panel). The duration of the action potentials was shortened and was associated with M-currents that were both higher in magnitude and shorter in duration compared with the WT (Fig. 10*A*, bottom panel). The increment in firing rate, however, depends on the location of the compartments expressing an increased M-current conductance, with the highest number of action potentials obtained when KCNQ2/3 GOF was expressed both at the soma and AIS (Fig. 10*B*).

Then, we investigated whether a nonuniform expression of the KCNQ GOF along the neuron compartments would influence the overall neuronal excitability. Specifically, we simultaneously expressed KCNQ GOF at the soma, AIS, and apical dendrite (*soma+AIS+apical* configuration) but differentially increased $g_{max}$ in the soma and apical dendrites compared with the AIS (i.e., 1.5 vs three times the value used in the control case; soma and apical vs AIS). Figure 10*C* shows that a nonuniform expression of the GOF at the soma versus the AIS can further decrease the postspike repolarization phase, thus increasing the firing rate compared to a uniform expression (compare Fig. 10*A* and 10*C*). This is further confirmed when comparing the maximum count of action potentials for the *soma+AIS+apical* configuration with uniform versus nonuniform GOF expression (Fig. 10*D*), where the differential increment in GOF at the AIS

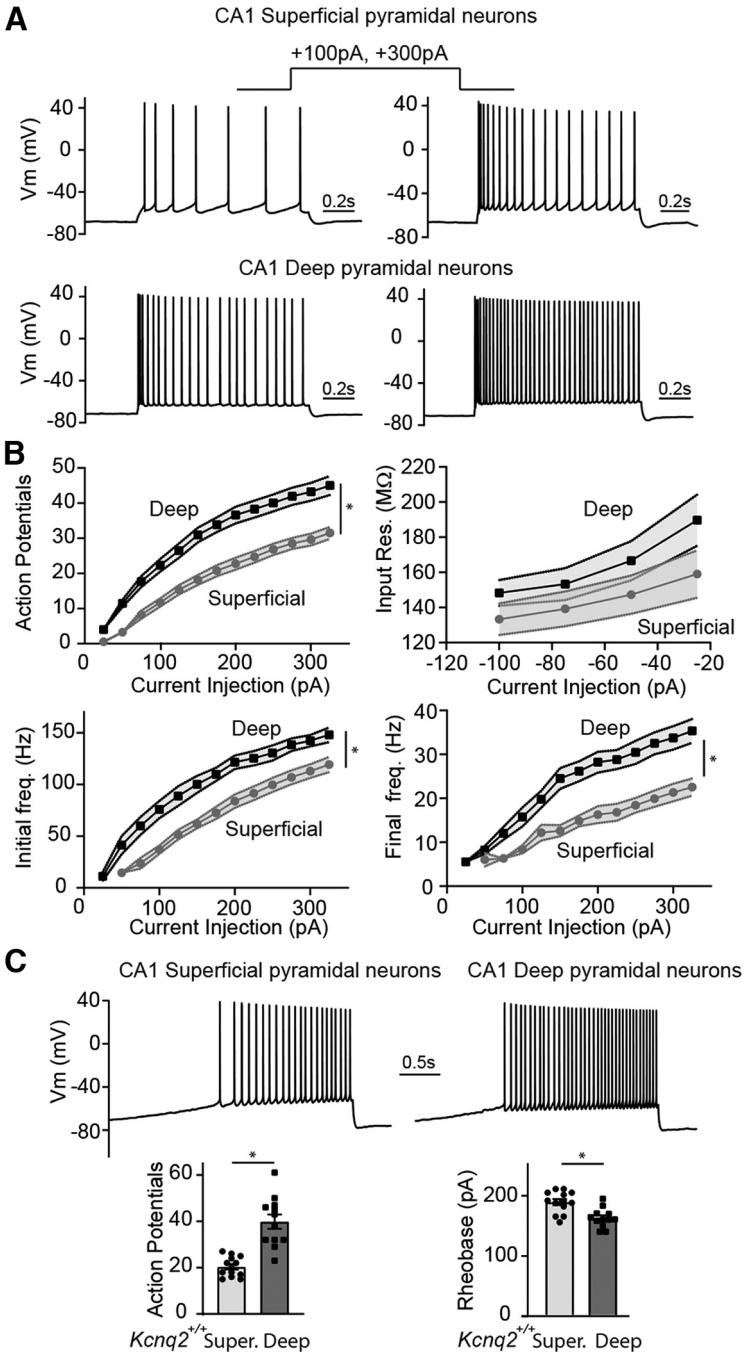


**Figure 6.** Superficial and Deep CA1 pyramidal neurons have distinct firing properties. ***A***, Representative traces of a voltage response to step current injections to +100 and +300 pA in superficial (top) and deep (bottom) dorsal CA1a pyramidal neurons. ***B***, Summary graphs comparing action potential count, initial and final frequency and input resistance between deep and superficial CA1a pyramidal neurons. ***C***, Top, Representative traces of voltage responses of deep (left) and superficial (right) CA1a pyramidal neurons to slow ramps (+120 pA/s). Bottom, Summary graphs of ramp action potential count and rheobase (Deep: $n = 13$, $N = 7$; Superficial: $n = 14$, $N = 8$). Summary graphs show mean and SEM. * indicates $p < 0.05$. Detailed statistics are found in Table 2.

shifts the AP-I curve rightward and increases the average firing rate across the step current values.

To gain a better understanding of the effects of M-current GOF, we conducted an analysis of the action potential rise and decay rate. Our simulations revealed that M-current GOF had limited effect on the rate of rise of the action potentials. However, the rate of action potential decay shifted toward faster values in models with GOF variants, an effect most pronounced in cases where M-currents were uniformly distributed, compared with scenarios where the maximum conductance of M-current was reduced solely in the soma as opposed to the AIS. Overall, the changes in the action potential waveform would result in greater sodium channel availability, especially for high-amplitude step currents, which would lead to a higher number of action potentials fired per unit of time.

Thus, our modeling suggests that increased firing frequency secondary to KCNQ2/3 GOF might stem from a larger number of open M-channels during the action potential, faster kinetics at 30°C, and a high AIS input resistance, which altogether enabled the M-current to contribute to the action potential repolarization. As predicted by the model, we found an increase in action potential decay in $KCNQ3^{R231C}$-expressing L2/3 pyramidal

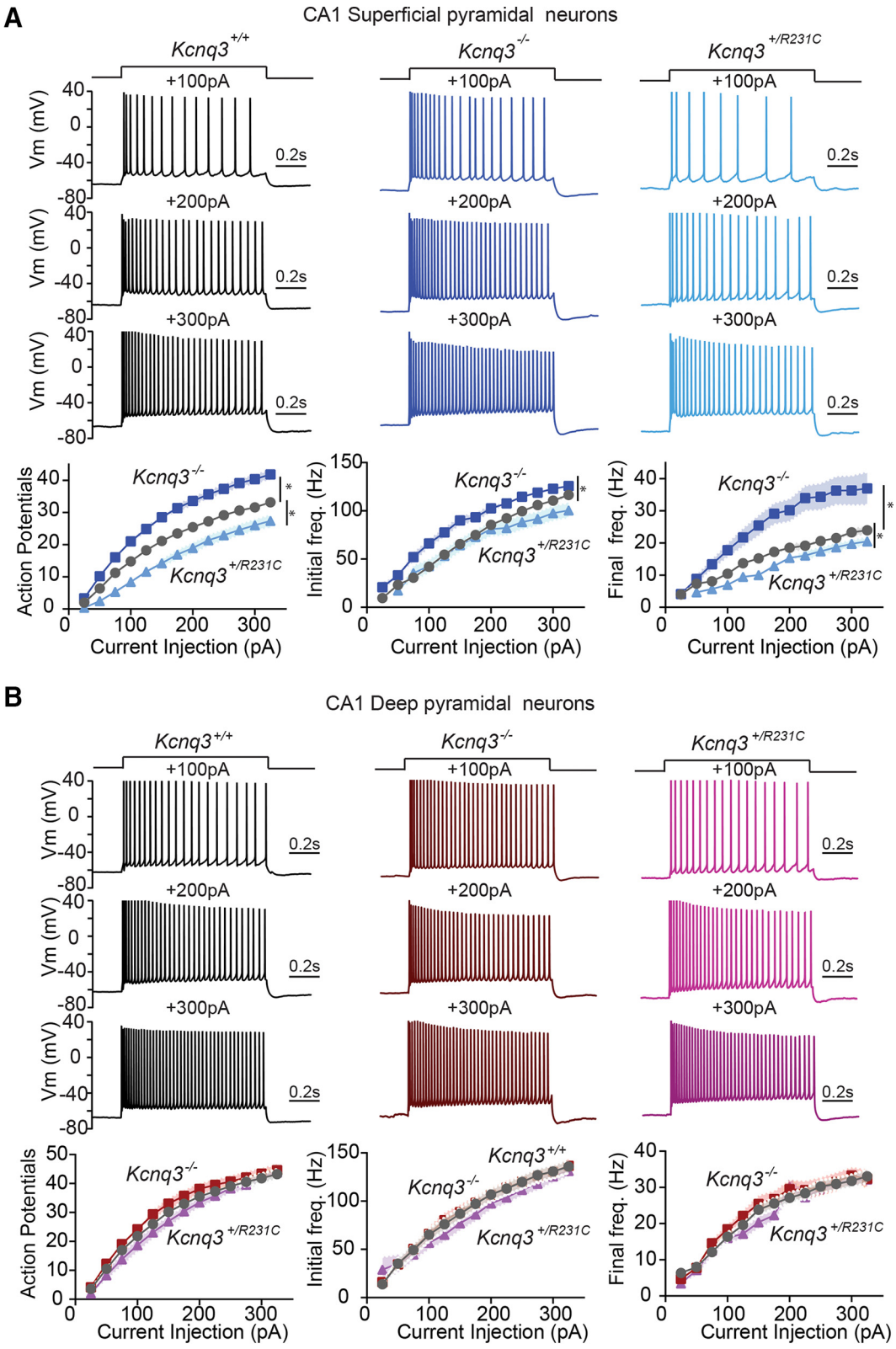


**Figure 7.** KCNQ3 channels preferentially control the firing properties of Superficial CA1 pyramidal neurons. ***A***, Representative traces of step current injections of +100, +200, and +300 pA in CA1a superficial pyramidal neurons of the hippocampus from *Kcnq3*$^{+/+}$, constitutive *Kcnq3* knock-out (*Kcnq3*−/−), and constitutive *Kcnq3*$^{R231C}$ (*Kcnq3*$^{+/R231C}$) knock-in mice. Summary graphs show the action potential count, initial and final frequency between these genotypes (*Kcnq3*$^{+/+}$: $n = 27$, $N = 13$; *Kcnq3*−/−: $n = 16$, $N = 6$; *Kcnq3*$^{+/R231C}$: $n = 17$, $N = 7$). Gray filled circles indicate recordings from *Kcnq3*$^{+/+}$ mice. ***B***, Representative traces showing deep CA1a pyramidal neuron voltage responses in response to +100-, +200-, or +300-pA current injections from *Kcnq3*$^{+/+}$, *Kcnq3*−/−, and *Kcnq3*$^{+/R231C}$ mice (*Kcnq3*$^{+/+}$: $n = 25$, $N = 14$; *Kcnq3*−/−: $n = 15$, $N = 6$; *Kcnq3*$^{+/R231C}$: $n = 16$, $N = 8$). Gray filled circles indicate recordings from *Kcnq3*$^{+/+}$ mice. Summary graphs show the action potential count, initial and final frequency between these genotypes. Summary graphs show mean and SEM. * indicates $p < 0.05$. Detailed statistics are found in Table 2.

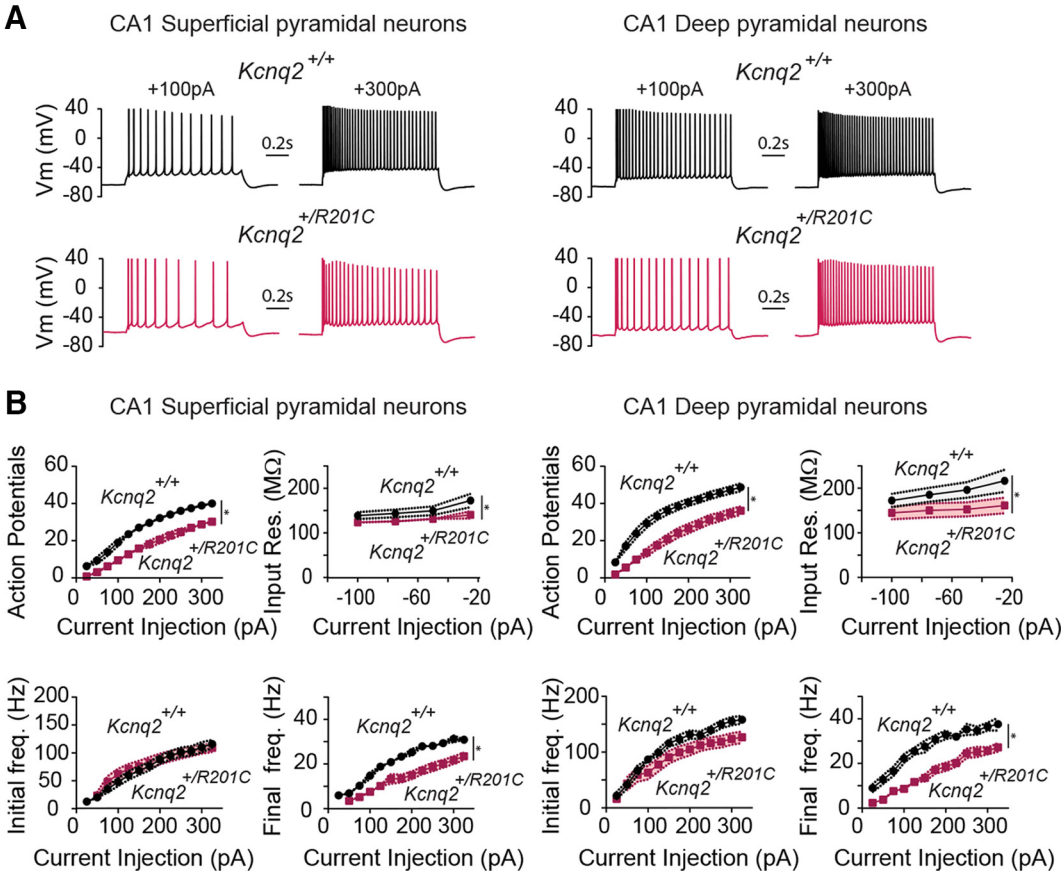


**Figure 8.** Expression of $Kcnq2^{R201C}$ dampens excitability of CA1 pyramidal neurons independent of radial layer. ***A***, Representative traces of voltage responses to +100- and +300-pA step current injections in CA1a superficial pyramidal neurons (left) and CA1a deep pyramidal neurons (right) of the hippocampus. ***B***, Left, Summary graphs of action potential count, initial, final frequency and input resistance of CA1a superficial pyramidal neurons. Right, summary graphs of action potential count, initial frequency, final frequency, and input resistance of CA1 deep neurons (Deep: $Kcnq2^{+/+}$: $n = 10$, $N = 5$; $Kcnq2^{+/R201C}$: $n = 10$, $N = 4$; Superficial: $Kcnq2^{+/+}$: $n = 11$, $N = 4$; $Kcnq2^{+/R201C}$: $n = 13$, $N = 4$). Summary graphs show mean and SEM. * indicates $p < 0.05$. Detailed statistics are found in Table 2.

neurons (dv/dt decay: $Kcnq3^{+/+}$ $-44 \pm 1.7$ mV/ms, $n = 11$, $N = 3$; $Kcnq3^{+/R231C}$ $-53 \pm 2.5$ mV/ms, $n = 12$, $N = 3$; $p = 0.004$, $t = 3.25$, df = 21, Student's $t$ test) as well as in $KCNQ2^{R201C}$ L2/3 pyramidal neurons (dv/dt decay: $Kcnq2^{+/+}$ $-55 \pm 2.41$ mV/ms, $n = 11$, $N = 3$; $Kcnq2^{+/R201C}$ $-61 \pm 2.5$ mV/ms, $n = 10$, $N = 3$; $p = 0.10$, $t = 1.72$, df = 19, Student's $t$ test). However, the model also predicts that the rheobase should increase with an increase in the M-current, which is contrary to our experimental findings showing a decrease in the rheobase. Accordingly, it is plausible that additional effects not explicitly accounted for in our model may also contribute to the shift in neuronal excitability. These effects, e.g., secondary to homeostatic intrinsic plasticity, would co-occur along with the increment of M-current and further contribute to hyperexcitability by decreasing the rheobase value or alter action potential properties. Indeed, unlike suggestions of the model, we found that the rate of action potential rise is significantly increased in the presence of KCNQ2/3 GOF (dv/dt rise: $Kcnq2^{+/+}$ $267 \pm 14$ mV/ms, $n = 11$, $N = 3$; $Kcnq2^{+/R201C}$ $317 \pm 15$ mV/ms, $n = 10$, $N = 3$; $p = 0.026$, $t = 2.4$, df = 19, Student's $t$ test) and $KCNQ3^{R231C}$ (dv/dt rise: $Kcnq3^{+/+}$ $193 \pm 10$ mV/ms, $n = 11$, $N = 3$; $Kcnq3^{+/R231C}$ $249 \pm 13$ mV/ms, $n = 12$, $N = 3$; $p = 0.003$, $t = 3.36$, df = 21, Student's $t$ test). In contrast, no such change was observed in CA1 pyramidal neurons (dv/dt rise: $Kcnq2^{+/+}$ $340 \pm 18$ mV/ms, $n = 23$, $N = 8$; $Kcnq2^{+/R201C}$ $354 \pm 25$ mV/ms, $n = 19$, $N = 4$) and $KCNQ3^{R231C}$ (dv/dt rise: $Kcnq3^{+/+}$ $409 \pm 19$ mV/ms, $n = 25$, $N = 14$; $Kcnq3^{+/R231C}$ $400 \pm 22$ mV/ms, $n = 16$, $N = 8$).

## Discussion

The traditional assumption is that a given KCNQ2 or KCNQ3 pathogenic variant would have a uniform effect on neuronal excitability, regardless of the specific pyramidal neuron cell type, region, or subregion. However, our study challenges this view by demonstrating that KCNQ2 and KCNQ3 GOF variants can modulate pyramidal neuron excitability in a region-specific manner. Additionally, our findings using *Kcnq3* knock-out and $Kcnq3^{+/R231C}$ GOF mice reveal an unanticipated role of KCNQ3 channels in regulating the excitability of CA1 pyramidal neurons differentially between the superficial and deep layers. Thus, our work has revealed a new level of complexity in the function of KCNQ2 and KCNQ3 channels in the forebrain.

One of the most puzzling discoveries in recent years was the realization that hyperexcitability can result from GOF variants in the KCNQ2 and KCNQ3 potassium channels (Niday and Tzingounis, 2018). The prevailing view is that such GOF variants are likely to suppress interneurons, leading to disinhibition and network hypersynchrony (Miceli et al., 2015). This hypothesis is supported by *in silico* studies suggesting that interneurons, because of their higher input resistance, are more vulnerable to KCNQ2/3 GOF variants than pyramidal neurons (Miceli et al., 2015). However, this assumption overlooks the fact that different pyramidal neurons express distinct sets of ion channels and have unique membrane properties, and hence may not all act similarly in response to KCNQ2/3 GOF variants.

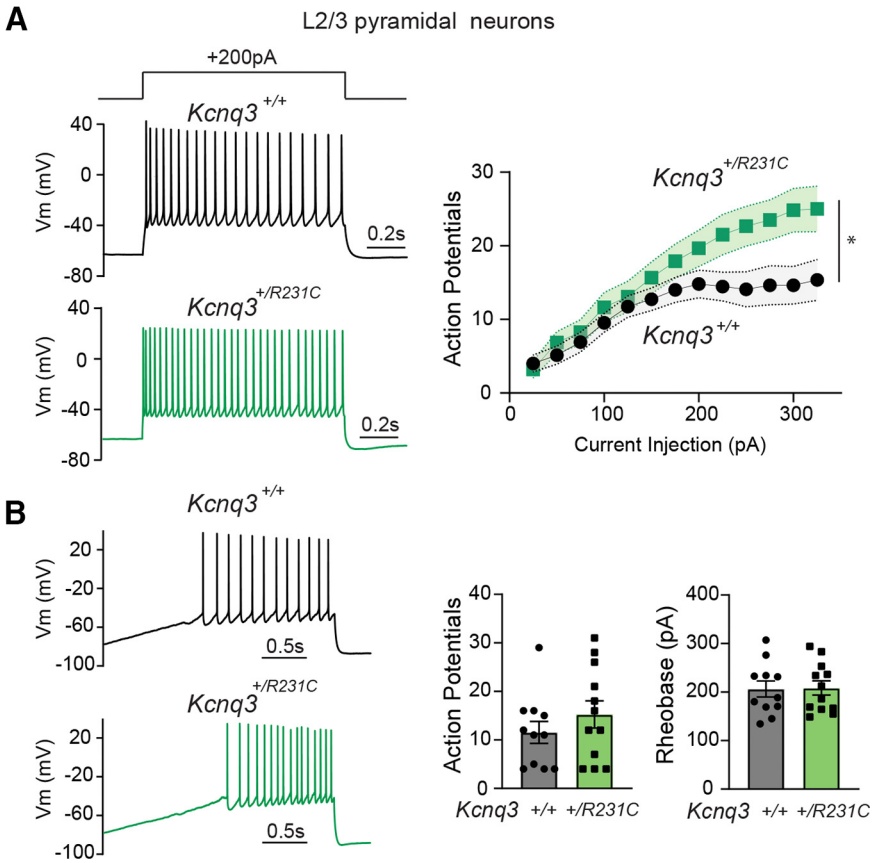


**Figure 9.** KCNQ3$^{R231C}$ increases the excitability of L2/3 pyramidal neurons. ***A***, Left, Representative traces of voltage responses to +200-pA step current injection from layer 2/3 pyramidal neurons of the somatosensory cortex. Right, Summary graph of action potential count. ***B***, Left, Representative traces of voltage responses to ramp current protocol (+120 pA/s). Right, summary graphs of action potential count and rheobase current (*Kcnq3*$^{+/+}$: $n = 11$, $N = 3$; *Kcnq3*$^{+/R231C}$: $n = 12$, $N = 3$). Summary graphs show mean and SEM. * indicates $p < 0.05$. Detailed statistics are found in Table 2.

Indeed, our simulations showed that increasing the M-current conductance in L2/3 pyramidal neurons results in a higher firing rate than predicted. This unexpected result is possibly because of the fact that the increased number of open M-current channels during the action potential allows them to contribute to the temporal profile of the action potential. Although a substantial amount of additional KCNQ2/3 and M-channels might not open during an action potential, the channels that are already open can act as a leak potassium current, increasing potassium flux as the potassium-driving forces become greater during an action potential. Additionally, a higher M-current density could accelerate the relief of sodium channel inactivation by hyperpolarizing the AIS membrane potential, thus accelerating the firing frequency of pyramidal neurons.

Although our simulations offer a plausible rationale for the elevated firing frequency observed in L2/3 pyramidal neurons, they do not account for the reduction in rheobase that we found using multiple stimulation protocols. Indeed, numerous studies have demonstrated that extended periods of inactivity can trigger homeostatic adjustments that lower the density of potassium channels (Desai et al., 1999; Turrigiano, 2012), especially those that govern rheobase. We speculate that early in the development of L2/3 pyramidal neurons, KCNQ2 and KCNQ3 GOF variants reduce their activity, thereby initiating a cascade of homeostatic adaptations that would decrease their rheobase. Such a mechanism might provide an explanation for the infantile development of seizures in patients with KCNQ2 and KCNQ3 GOF variants (Mulkey et al., 2017; Sands et al., 2019; Miceli et al., 2022), unlike the appearance of seizures soon after birth in patients with KCNQ2/3 LOF variants (Weckhuysen et al., 2012; Millichap et al., 2016). Further work is necessary, across multiple developmental time points, to identify the specific potassium channels that may be altered and whether changes in KCNQ2/3 GOF also affect the location of the AIS and voltage-gated sodium channel distribution and levels (see below).

One key question that arises from this work is why CA1 pyramidal neurons do not become hyperexcitable and instead exhibit hypoexcitability. This effect is likely influenced by various factors, such as the type of voltage-gated sodium, calcium, and potassium channels present in CA1 pyramidal neurons and the density of KCNQ2/3 channels across these neurons during development. For instance, L2/3 pyramidal neurons express KCNQ2/3 channels across all neuronal compartments including dendrites and axons (Galvin et al., 2020), unlike KCNQ2/3 expression in CA1 pyramidal neurons, which is primarily restricted to axons and to a lesser degree in the soma (Devaux et al., 2004; Pan et al., 2006). This difference in channel expression raises the possibility that KCNQ2/3 GOF variants could have varying effects on excitability across different compartments of the neuron. Thus, the presence of KCNQ2/3 GOF may lead to a dampening of excitability across all compartments of pyramidal neurons, including the soma, axon initial segment (AIS), and dendrites. This modulation of excitability triggered by KCNQ2/3 GOF variants might initiate a distinct homeostatic plasticity program in L2/3 pyramidal neurons compared with CA1 pyramidal neurons. Indeed, we observed that L2/3 pyramidal neurons expressing KCNQ2/3

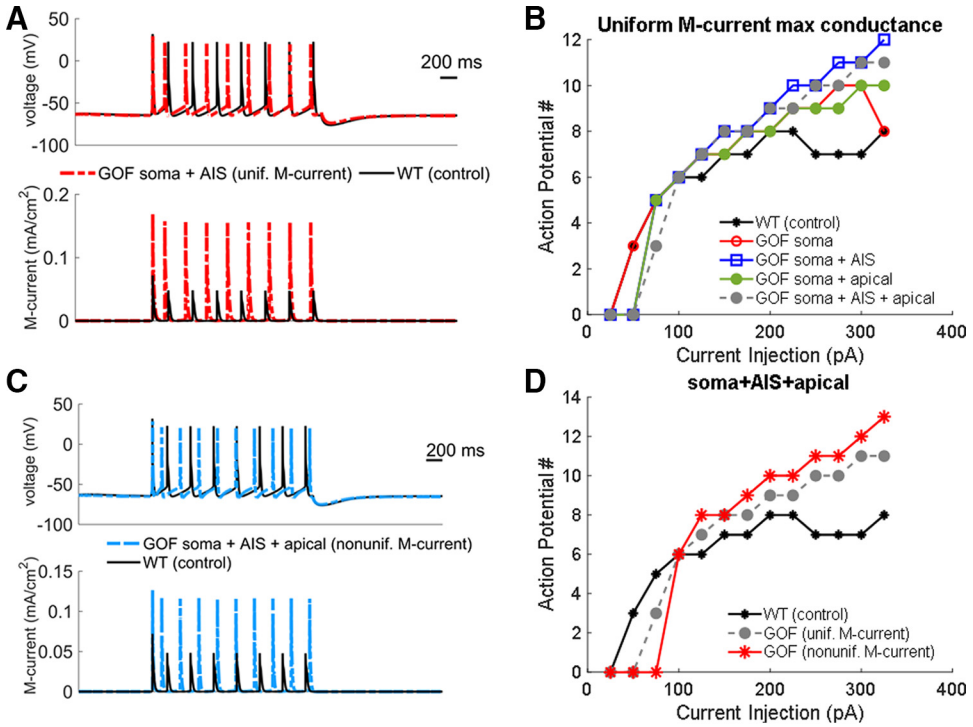


**Figure 10.** KCNQ2/3 gain-of-function increased neuronal excitability of pyramidal neurons *in silico*. ***A***, Response of the L2/3 pyramidal neuron model to a +200-pA step current to the soma in case of WT (control case, black lines) and KCNQ2/3 GOF (red lines). In this model, KCNQ2/3 GOF changes only occur at soma and AIS. Top panel, Transmembrane voltage at the soma in response to the current step. Bottom panel, Somatic M-current density in response to the current step. ***B***, Action potential-to-current curve estimated for the neuron model in the control WT case (black line) and KCNQ2/3 GOF. KCNQ2/3 GOF is alternatively paired with increased conductance $g_{max}$ (uniform values) at the soma (red line), soma+AIS (blue line), soma+apical dendrite (green line), or soma+AIS+apical dendrite (gray line). ***C***, Response of the L2/3 pyramidal neuron model to a +200-pA step current to the soma in the control WT case (black lines) and KCNQ2/3 GOF (blue lines). In this model, KCNQ2/3 GOF occurs at soma, AIS, and apical dendrite, with nonuniform M-current distribution, i.e., M-current density at the AIS is higher than the value at the soma and apical dendrite (values as in panel ***D***). Top panel, Transmembrane voltage at the soma in response to the current step. Bottom panel, Somatic M-current density in response to the current step. ***D***, Action potential-to-current curve estimated for the neuron model in the control WT case (black line) and KCNQ2/3 GOF with increased conductance $g_{max}$ of the M-channels at soma, AIS, and apical dendrite. Both uniform assignments (gray line) and nonuniform assignments (red line) to the value of $g_{max}$ across compartments are depicted. Nonuniform indicates that the M-current density at the AIS is higher than the value at the soma and apical dendrites (i.e., 3× vs 1.5× the value used in control case). In all simulations, step currents started at $t = 500$ ms and lasted 1000 ms.

gain-of-function (GOF) channels exhibited a significantly higher rate of action potential depolarization compared with wild-type pyramidal neurons. In contrast, in CA1 pyramidal neurons, the presence of KCNQ2/3 GOF channels did not have any substantial effect on the rate of action potential depolarization. This elevated rate of action potential depolarization typically correlates with voltage-gated sodium channel availability, indicating either an increased expression of these channels or reduced resting inactivation, effects that could potentially counteract any reduced L2/3 pyramidal neuron excitability occurring earlier in development. Upregulation of voltage-gated sodium channels in response to prolonged dampened excitability by increased potassium channel activity has been documented in previous studies (Pratt and Aizenman, 2007), suggesting a possible adaptive mechanism in neurons. Regardless of the exact mechanisms responsible for the contrasting effects observed in CA1 and L2/3 pyramidal neurons, our data suggest that the presence of KCNQ2/3 gain-of-function (GOF) channels clamps the CA1 pyramidal neuron membrane potential close to rest. As a result, greater input currents would be necessary to counteract the inhibitory effect imposed by KCNQ2/3 GOF channels. Our data support this idea, as the expression of $Kcnq2^{R201C}$ resulted in higher rheobase compared with control neurons.

More recently, research has suggested that KCNQ3 GOF variants could lead to the appearance of a gating pore current when KCNQ3 channels are closed (Gamal El-Din et al., 2021). Such a gating pore current might act as a shunt, dampening excitability (Gamal El-Din et al., 2021). As with L2/3 pyramidal neurons, a more thorough investigation across development is necessary to fully understand how KCNQ2/3 GOF controls the activity of CA1 pyramidal neurons. It is worth noting that our work does not rule out a potential role of GABAergic interneurons in KCNQ2/3 GOF. Thus, likely, multiple cell types including both glutamatergic and GABAergic neurons contribute to the effect of KCNQ2/3 gain-of-function in the brain.

Our work using *Kcnq3* knock-out and $Kcnq3^{+/R231C}$ knock-in mice also provides a window into the role of KCNQ3 channels in regulating the properties of superficial layer CA1 pyramidal neurons. In recent years, it has become clear that CA1 pyramidal neurons can be divided into two distinct groups based on their firing properties, position in the radial axis, and transcriptomic signatures: deep and superficial layers (Valero et al., 2015; Cembrowski et al., 2016; Masurkar et al., 2020; Cid et al., 2021). These two groups have different inputs, outputs, and place cell properties (Soltesz and Losonczy, 2018). However, the ion channels that dictate the different firing behaviors between the two layers have remained elusive. Our findings suggest that KCNQ3 channels are critical potassium channels that determine the firing properties of the superficial layer pyramidal neurons. Increasing or decreasing the activity of KCNQ3 channels bi-directionally altered the firing properties of these neurons. This concept is

**Table 2. Summary of statistical tests**

| Figure | Type of test | *F*, or *t*, df | *p* value |
|---|---|---|---|
| Figure 2 | | | |
| 2*A*, action potential count | Two-way repeated measures ANOVA | $F_{(12, 237)} = 9.663$ | <0.0001 |
| 2*A*, initial frequency | Area under the curve, unpaired Student's *t* test | $t = 1.376$, df = 42 | 0.1763 |
| 2*A*, final frequency | Area under the curve, unpaired Student's *t* test | $t = 6.295$, df = 41 | <0.0001 |
| 2*A*, input resistance | Two-way repeated measures ANOVA | $F_{(3,58)} = 8.448$ | <0.0001 |
| 2*B*, ramp action potential count | Unpaired *t* test | $t = 4.969$, df = 40 | <0.0001 |
| 2*B*, ramp rheobase | Unpaired *t* test | $t = 0.5047$, df = 40 | 0.6166 |
| 2*C*, action potential number | Two-way repeated measures ANOVA | $F_{(12,106)} = 2.395$ | 0.0088 |
| 2*C*, initial frequency | Area under the curve, unpaired Student's *t* test | $t = 3.807$, df = 19 | 0.0012 |
| 2*C*, final frequency | Area under the curve, unpaired Student's *t* test | $t = 1.079$, df = 17 | 0.2954 |
| 2*C*, input resistance | Two-way repeated measures ANOVA | $F_{(3,26)} = 1.210$ | 0.3256 |
| 2*D*, ramp action potential count | Unpaired *t* test | $t = 2.342$, df = 19 | 0.0302 |
| 2*D*, ramp rheobase | Unpaired *t* test | $t = 3.421$, df = 19 | 0.0029 |
| Figure 3 | | | |
| 3*B*, CA1 1st wave action potential count | Two-way repeated measures ANOVA | $F_{(9,79)} = 11.45$ | <0.0001 |
| 3*B*, CA1 1st wave rheobase | Unpaired *t* test | $t = 2.672$, df = 20 | 0.0147 |
| 3*B*, CA1 4th wave action potential count | Two-way repeated measures ANOVA | $F_{(9,79)} = 9.726$ | <0.0001 |
| 3*B*, CA1 4th wave rheobase | Unpaired *t* test | $t = 3.501$, df = 19 | 0.0024 |
| 3*B*, L23 1st wave action potential count | Two-way repeated measures ANOVA | $F_{(9,71)} = 7.220$ | <0.0001 |
| 3*B*, L23 1st wave rheobase | Unpaired *t* test | $t = 3.049$, df = 18 | 0.0069 |
| 3*B*, L23 4th wave action potential count | Two-way repeated measures ANOVA | $F_{(9,70)} = 3.657$ | 0.0009 |
| 3*B*, L23 4th wave rheobase | Unpaired *t* test | $t = 2.618$, df = 18 | 0.0174 |
| Figure 4 | | | |
| 4*B*, I-XE991 | Unpaired *t* test | $t = 2.552$, df = 17 | 0.0206 |
| 4*B*, I-XE991 density | Unpaired *t* test | $t = 3.247$, df = 17 | 0.0047 |
| 4*B*, M current density | Unpaired *t* test | $t = 2.258$, df = 17 | 0.0374 |
| Figure 6 | | | |
| 6B, action potential count | Two-way repeated measures ANOVA | $F_{(12,143)} = 11.54$ | <0.0001 |
| 6B, initial frequency | Area under the curve, unpaired Student's *t* test | $t = 3.855$, df=23 | 0.0008 |
| 6B, final frequency | Area under the curve, unpaired Student's *t* test | $t = 4.283$, df=23 | 0.0003 |
| 6B, input resistance | Two-way repeated measures ANOVA | $F_{(3,35)} = 2.528$ | 0.0732 |
| 6C, ramp action potential count | Unpaired *t* test | $t = 6.055$, df=23 | <0.0001 |
| 6C, ramp rheobase | Unpaired *t* test | $t = 3.892$, df=23 | 0.0007 |
| Figure 7 | | | |
| 7*A*, superficial: $Kcnq3^{+/+}$ vs $Kcnq3^{-/-}$, action potential count | Two-way repeated measures ANOVA | $F_{(12,169)} = 9.476$ | <0.0001 |
| 7*A*, superficial: $Kcnq3^{+/+}$ vs $Kcnq3^{+/R231C}$, action potential count | Two-way repeated measures ANOVA | $F_{(12,182)} = 2.656$ | 0.0026 |
| 7*A*, superficial: $Kcnq3^{+/+}$ vs $Kcnq3^{-/-}$, initial frequency | Area under the curve, unpaired Student's *t* test | $t = 3.308$, df = 41 | 0.0020 |
| 7*A*, superficial: $Kcnq3^{+/+}$ vs $Kcnq3^{+/R231C}$, initial frequency | Area under the curve, unpaired Student's *t* test | $t = 1.294$, df = 42 | 0.2027 |
| 7*A*, superficial: $Kcnq3^{+/+}$ vs $Kcnq3^{-/-}$, final frequency | Area under the curve, unpaired Student's *t* test | $t = 3.627$, df = 39 | 0.0008 |
| 7*A*, superficial: $Kcnq3^{+/+}$ vs $Kcnq3^{+/R231C}$, final frequency | Area under the curve, unpaired Student's *t* test | $t = 2.395$, df = 40 | 0.0214 |
| 7*B*, deep: $Kcnq3^{+/+}$ vs $Kcnq3^{-/-}$, action potential | Two-way repeated measures ANOVA | $F_{(12,158)} = 0.8614$ | 0.5874 |
| 7*B*, deep: $Kcnq3^{+/+}$ vs $Kcnq3^{+/R231C}$, action potential | Two-way repeated measures ANOVA | $F_{(12,184)} = 1.292$ | 0.2260 |
| 7*B*, deep: $Kcnq3^{+/+}$ vs $Kcnq3^{-/-}$, initial frequency | Area under the curve, unpaired Student's *t* test | $t = 0.1078$, df = 36 | 0.9147 |
| 7*B*, deep: $Kcnq3^{+/+}$ vs $Kcnq3^{+/R231C}$, initial frequency | Area under the curve, unpaired Student's *t* test | $t = 0.9750$, df = 38 | 0.3357 |
| 7*B*, deep: $Kcnq3^{+/+}$ vs $Kcnq3^{-/-}$, final frequency | Area under the curve, unpaired Student's *t* test | $t = 0.6985$, df = 34 | 0.4896 |
| 7*B*, deep: $Kcnq3^{+/+}$ vs $Kcnq3^{+/R231C}$, final frequency | Area under the curve, unpaired Student's *t* test | $t = 0.7368$, df = 38 | 0.4658 |
| Figure 8 | | | |
| 8*B*, superficial: action potential count | Two-way repeated measures ANOVA | $F_{(12,118)} = 5.528$ | <0.0001 |
| 8*B*, superficial: initial frequency | Area under the curve, unpaired Student's *t* test | $t = 0.0048$, df=22 | 0.99 |
| 8*B*, superficial: final frequency | Area under the curve, unpaired Student's *t* test | $t = 4.831$, df=22 | <0.0001 |
| 8*B*, superficial: input resistance | Two-way repeated measures ANOVA | $F_{(3,28)} = 4.003$ | 0.0172 |
| 8*B*, deep: action potential count | Two-way repeated measures ANOVA | $F_{(12,107)} = 8.778$ | <0.0001 |
| 8*B*, deep: initial frequency | Area under the curve, unpaired Student's *t* test | $t = 2.060$, df=18 | 0.0541 |
| 8*B*, deep: final frequency | Area under the curve, unpaired Student's *t* test | $t = 5.213$, df=18 | <0.0001 |
| 8*B*, deep: input resistance | Two-way repeated measures ANOVA | $F_{(3,27)} = 4.543$ | 0.0106 |
| Figure 9 | | | |
| 9*A*, $Kcnq3^{+/R231C}$ action potential count | Two-way repeated measures ANOVA | $F_{(12,118)} = 7.686$ | <0.0001 |
| 9*B*, ramp action potential count | Unpaired *t* test | $t = 1.015$, df = 21 | 0.3219 |
| 9*B*, ramp rheobase | Unpaired *t* test | $t = 0.1050$, df = 21 | 0.9173 |

The table reports the different statistical tests performed for the different figure panels.

consistent with the observation that *Kcnq3* mRNA transcript levels are higher in superficial layer neurons than in deep layer neurons (Cembrowski et al., 2016; Cid et al., 2021). In contrast, *Kcnq2* mRNA levels are similar between the two layers (Cembrowski et al., 2016). KCNQ2 GOF dampened excitability in both layers and made the firing rate of the two layers more similar, decreasing heterogeneity of the firing properties between the layers. This decrease in heterogeneity could

potentially affect the computational power of the hippocampal network and make it more hyperexcitable (Rich et al., 2022). Further work is needed to understand the consequences of KCNQ2 and KCNQ3 pathogenic variants in hippocampal network function.

Taken together, we propose that pathogenic GOF variants in KCNQ2 and KCNQ3 can result in either hypoexcitability or hyperexcitability of pyramidal neurons. Therefore, understanding the relationship between genotype and phenotype of KCNQ2 and KCNQ3 pathogenic variants requires analyzing multiple cell types and regions.

## References


Allen NM, Weckhuysen S, Gorman K, King MD, Lerche H (2020) Genetic potassium channel-associated epilepsies: clinical review of the $K_V$ family. Eur J Paediatr Neurol 24:105–116.

Battefeld A, Tran BT, Gavrilis J, Cooper EC, Kole MH (2014) Heteromeric Kv7.2/7.3 channels differentially regulate action potential initiation and conduction in neocortical myelinated axons. J Neurosci 34:3719–3732.

Boets S, Johannesen KM, Destree A, Manti F, Ramantani G, Lesca G, Vercueil L, Koenig MK, Striano P, Møller RS, Cooper E, Weckhuysen S (2022) Adult phenotype of KCNQ2 encephalopathy. J Med Genet 59:528–535.

Carnevale NT, Hines ML (2006) The NEURON book. Cambridge: Cambridge University Press.

Cembrowski MS, Wang L, Sugino K, Shields BC, Spruston N (2016) Hipposeq: a comprehensive RNA-seq database of gene expression in hippocampal principal neurons. Elife 5:e14997.

Cid E, Marquez-Galera A, Valero M, Gal B, Medeiros DC, Navarron CM, Ballesteros-Esteban L, Reig-Viader R, Morales AV, Fernandez-Lamo I, Gomez-Dominguez D, Sato M, Hayashi Y, Bayés À, Barco A, Lopez-Atalaya JP, de la Prida LM (2021) Sublayer- and cell-type-specific neurodegenerative transcriptional trajectories in hippocampal sclerosis. Cell Rep 35:109229.

Delorme A, Makeig S (2004) EEGLAB: an open source toolbox for analysis of single-trial EEG dynamics including independent component analysis. J Neurosci Methods 134:9–21.

Desai NS, Rutherford LC, Turrigiano GG (1999) Plasticity in the intrinsic excitability of cortical pyramidal neurons. Nat Neurosci 2:515–520.

Devaux JJ, Kleopa KA, Cooper EC, Scherer SS (2004) KCNQ2 is a nodal K+ channel. J Neurosci 24:1236–1244.

Dirkx N, Miceli F, Taglialatela M, Weckhuysen S (2020) The role of Kv7.2 in neurodevelopment: insights and gaps in our understanding. Front Physiol 11:570588.

Druckmann S, Banitt Y, Gidon A, Schürmann F, Markram H, Segev I (2007) A novel multiple objective optimization framework for constraining conductance-based neuron models by experimental data. Front Neurosci 1:7–18.

Galvin VC, Yang ST, Paspalas CD, Yang Y, Jin LE, Datta D, Morozov YM, Lightbourne TC, Lowet AS, Rakic P, Arnsten AFT, Wang M (2020) Muscarinic M1 receptors modulate working memory performance and activity via KCNQ potassium channels in the primate prefrontal cortex. Neuron 106:649–661.e4.

Gamal El-Din TM, Lantin T, Tschumi CW, Juarez B, Quinlan M, Hayano JH, Li J, Zweifel LS, Catterall WA (2021) Autism-associated mutations in KV7 channels induce gating pore current. Proc Natl Acad Sci U S A 118: e2112666118.

Gao X, Bender F, Soh H, Chen C, Altafi M, Schütze S, Heidenreich M, Gorbati M, Corbu MA, Carus-Cadavieco M, Korotkova T, Tzingounis AV, Jentsch TJ, Ponomarenko A (2021) Place fields of single spikes in hippocampus involve Kcnq3 channel-dependent entrainment of complex spike bursts. Nat Commun 12:4801.

Gorski JA, Talley T, Qiu M, Puelles L, Rubenstein JL, Jones KR (2002) Cortical excitatory neurons and glia, but not GABAergic neurons, are produced in the Emx1-expressing lineage. J Neurosci 22:6309–6314.

Heyne HO, et al. (2018) De novo variants in neurodevelopmental disorders with epilepsy. Nat Genet 50:1048–1053.

Jing J, Dunbar C, Sonesra A, Chavez A, Park S, Yang R, Soh H, Lee M, Tzingounis AV, Cooper EC, Jiang X, Maheshwari A (2022) Removal of KCNQ2 from parvalbumin-expressing interneurons improves anti-seizure efficacy of retigabine. Exp Neurol 355:114141.

Kim KS, Duignan KM, Hawryluk JM, Soh H, Tzingounis AV (2016) The voltage activation of cortical KCNQ channels depends on global PIP2 levels. Biophys J 110:1089–1098.

Li S, Choi V, Tzounopoulos T (2013) Pathogenic plasticity of Kv7.2/3 channel activity is essential for the induction of tinnitus. Proc Natl Acad Sci U S A 110:9980–9985.

Maheshwari A, Noebels JL (2014) Monogenic models of absence epilepsy: windows into the complex balance between inhibition and excitation in thalamocortical microcircuits. Prog Brain Res 213:223–252.

Malerba F, et al. (2020) Genotype-phenotype correlations in patients with de novo KCNQ2 pathogenic variants. Neurol Genet 6:e528.

Markram H, et al. (2015) Reconstruction and simulation of neocortical microcircuitry. Cell 163:456–492.

Masurkar AV, Tian C, Warren R, Reyes I, Lowes DC, Brann DH, Siegelbaum SA (2020) Postsynaptic integrative properties of dorsal CA1 pyramidal neuron subpopulations. J Neurophysiol 123:980–992.

Miceli F, Soldovieri MV, Ambrosino P, De Maria M, Migliore M, Migliore R, Taglialatela M (2015) Early-onset epileptic encephalopathy caused by gain-of-function mutations in the voltage sensor of Kv7.2 and Kv7.3 potassium channel subunits. J Neurosci 35:3782–3793.

Miceli F, et al. (2022) KCNQ2 R144 variants cause neurodevelopmental disability with language impairment and autistic features without neonatal seizures through a gain-of-function mechanism. EBioMedicine 81:104130.

Millichap JJ, et al. (2016) KCNQ2 encephalopathy: features, mutational hot spots, and ezogabine treatment of 11 patients. Neurol Genet 2:e96.

Mulkey SB, Ben-Zeev B, Nicolai J, Carroll JL, Grønborg S, Jiang YH, Joshi N, Kelly M, Koolen DA, Mikati MA, Park K, Pearl PL, Scheffer IE, Spillmann RC, Taglialatela M, Vieker S, Weckhuysen S, Cooper EC, Cilio MR (2017) Neonatal nonepileptic myoclonus is a prominent clinical feature of KCNQ2 gain-of-function variants R201C and R201H. Epilepsia 58:436–445.

Nappi P, Miceli F, Soldovieri MV, Ambrosino P, Barrese V, Taglialatela M (2020) Epileptic channelopathies caused by neuronal Kv7 (KCNQ) channel dysfunction. Pflugers Arch 472:881–898.

Niday Z, Tzingounis AV (2018) Potassium channel gain of function in epilepsy: an unresolved paradox. Neuroscientist 24:368–380.

Niday Z, Hawkins VE, Soh H, Mulkey DK, Tzingounis AV (2017) Epilepsy-associated KCNQ2 channels regulate multiple intrinsic properties of layer 2/3 pyramidal neurons. J Neurosci 37:576–586.

Pan Z, Kao T, Horvath Z, Lemos J, Sul JY, Cranstoun SD, Bennett V, Scherer SS, Cooper EC (2006) A common ankyrin-G-based mechanism retains KCNQ and NaV channels at electrically active domains of the axon. J Neurosci 26:2599–2613.

Pratt KG, Aizenman CD (2007) Homeostatic regulation of intrinsic excitability and synaptic transmission in a developing visual circuit. J Neurosci 27:8268–8277.

Ramaswamy S, et al. (2015) The neocortical microcircuit collaboration portal: a resource for rat somatosensory cortex. Front Neural Circuits 9:44.

Rich S, Moradi Chameh H, Lefebvre J, Valiante TA (2022) Loss of neuronal heterogeneity in epileptogenic human tissue impairs network resilience to sudden changes in synchrony. Cell Rep 39:110863.

Robbins J, Passmore GM, Abogadie FC, Reilly JM, Brown DA (2013) Effects of KCNQ2 gene truncation on M-type Kv7 potassium currents. PLoS One 8:e71809.

Sands TT, et al. (2019) Autism and developmental disability caused by KCNQ3 gain-of-function variants. Ann Neurol 86:181–192.

Satterstrom FK, et al. (2020) Large-scale exome sequencing study implicates both developmental and functional changes in the neurobiology of autism. Cell 180:568–584.e23.

Soh H, Pant R, LoTurco JJ, Tzingounis AV (2014) Conditional deletions of epilepsy-associated KCNQ2 and KCNQ3 channels from cerebral cortex cause differential effects on neuronal excitability. J Neurosci 34:5311–5321.

Soh H, Park S, Ryan K, Springer K, Maheshwari A, Tzingounis AV (2018) Deletion of KCNQ2/3 potassium channels from PV+ interneurons leads to homeostatic potentiation of excitatory transmission. Elife 7:e38617.

Soltesz I, Losonczy A (2018) CA1 pyramidal cell diversity enabling parallel information processing in the hippocampus. Nat Neurosci 21:484–493.

Timofeev I, Grenier F, Steriade M (1998) Spike-wave complexes and fast components of cortically generated seizures. IV. Paroxysmal fast runs in cortical and thalamic neurons. J Neurophysiol 80:1495–1513.

Turrigiano G (2012) Homeostatic synaptic plasticity: local and global mechanisms for stabilizing neuronal function. Cold Spring Harb Perspect Biol 4:a005736.

Valero M, Cid E, Averkin RG, Aguilar J, Sanchez-Aguilera A, Viney TJ, Gomez-Dominguez D, Bellistri E, de la Prida LM (2015) Determinants of different deep and superficial CA1 pyramidal cell dynamics during sharp-wave ripples. Nat Neurosci 18:1281–1290.

Wainger BJ, Kiskinis E, Mellin C, Wiskow O, Han SS, Sandoe J, Perez NP, Williams LA, Lee S, Boulting G, Berry JD, Brown RH Jr, Cudkowicz ME, Bean BP, Eggan K, Woolf CJ (2014) Intrinsic membrane hyperexcitability of amyotrophic lateral sclerosis patient-derived motor neurons. Cell Rep 7:1–11.

Wang T, et al. (2020) Large-scale targeted sequencing identifies risk genes for neurodevelopmental disorders. Nat Commun 11:4932.

Weckhuysen S, et al. (2012) KCNQ2 encephalopathy: emerging phenotype of a neonatal epileptic encephalopathy. Ann Neurol 71:15–25.

You JC, Muralidharan K, Park JW, Petrof I, Pyfer MS, Corbett BF, LaFrancois JJ, Zheng Y, Zhang X, Mohila CA, Yoshor D, Rissman RA, Nestler EJ, Scharfman HE, Chin J (2017) Epigenetic suppression of hippocampal calbindin-D28k by ΔFosB drives seizure-related cognitive deficits. Nat Med 23:1377–1383.